Mater Renew Sustain Energy (2016) 5:18
DOI 10.1007/s40243-016-0083-z

REVIEW PAPER

Tantalum nitride for photocatalytic water splitting: concept and applications

Ela Nurlaela[1] · Ahmed Ziani[1] · Kazuhiro Takanabe[1]

Received: 19 August 2016 / Accepted: 20 September 2016 / Published online: 12 October 2016

Abstract Along with many other solar energy conversion processes, research on photocatalytic water splitting to generate hydrogen and oxygen has experienced rapid major development over the past years. Developing an efficient visible-light-responsive photocatalyst has been one of the targets of such research efforts. In this regard, nitride materials, particularly Ta_3N_5, have been the subject of investigation due to their promising properties. This review focuses on the fundamental parameters involved in the photocatalytic processes targeting overall water splitting using Ta_3N_5 as a model photocatalyst. The discussion primarily focuses on relevant parameters that are involved in photon absorption, exciton separation, carrier diffusion, carrier transport, catalytic efficiency, and mass transfer of the reactants. An overview of collaborative experimental and theoretical approaches to achieve efficient photocatalytic water splitting using Ta_3N_5 is discussed.

Keywords Ta_3N_5 · Water splitting · Photocatalysis · Crystal structure · Optoelectronic properties · Kinetics · Carrier dynamic · Interface · Oxygen evolution reaction

Introduction

The development of new clean and inexpensive energy resources as an alternative to conventional fossil fuel energy is a crucial challenge for the scientific community. Solar H_2O splitting is one of the most innovative solutions that have emerged over the past years [1–8]. H_2 production can currently be achieved through an artificial photosynthetic way, in the UV domain, using broad bandgap photocatalyst materials such as TiO_2 [9] or using photoactive oxides such as α-Fe_2O_3, WO_3 or $BiVO_4$ under visible light irradiation (1.7–2.8 eV) [10–15]. However, these types of materials are effective only for half of the reaction (water oxidation). For overall water splitting, there is a limited choice of photocatalysts, such as Ta_3N_5, TaON, or some material from the family of oxynitride perovskites [16–24]. Achieving one step overall water splitting with one single photocatalyst presents a practical way in term of engineering design of the reactions. The simplicity of using powder semiconductor photocatalysis makes this technique economically feasible for its scalability and capital cost. Thanks to its extended visible absorption (600 nm) and its ability for the redox reaction, Ta_3N_5 is an attractive photocatalyst that can theoretically achieve a solar energy to hydrogen conversion efficiency of $\sim$17 %. Many studies have addressed improving the photocurrent at the potential for water oxidation [20–24]. A significant photocurrent can be achieved by increasing the structuration of the photocatalyst and using a high-performance cocatalyst, but understanding the intrinsic properties of Ta_3N_5 for obtaining a significant improvement in the global photoelectrocatalytic reaction is still a challenge. Knowledge of the material's intrinsic properties can help to improve the photocatalytic performance.

Photocatalytic water splitting mechanism

The basic principle of photocatalytic water splitting is schematically depicted in Fig. 1. The reaction begins when the photocatalyst absorbs light with a photon energy

✉ Kazuhiro Takanabe
kazuhiro.takanabe@kaust.edu.sa

[1] KAUST Catalysis Center and Physical Sciences and Engineering Division (PSE), King Abdullah University of Science and Technology (KAUST), 4700 KAUST, Thuwal 23955-6900, Saudi Arabia

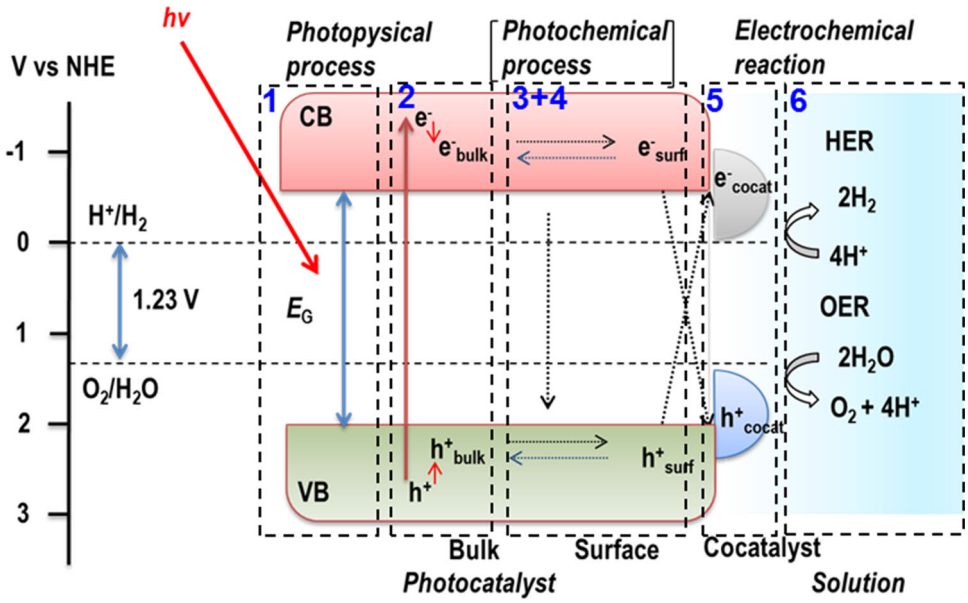

Fig. 1 Schematic of processes involved in photocatalytic water splitting. The steps involved in the photocatalysis for water splitting process are presented in the scheme: *1* photon absorption, *2* exciton separation, *3* carrier diffusion, *4* carrier transport, *5* catalytic efficiency, and *6* mass transfer of reactants

that is higher than its bandgap [7, 8, 18, 25–28]. This process initiates electron excitation from the valence band (VB) to the conduction band (CB), simultaneously leaving a hole in the valence band. This initiation proceeds in a very short time (at the femtosecond scale), followed by relaxation of the hole to the bottom of the CB and to the top of the VB, respectively, on a similar time scale. Furthermore, the photogenerated charges will undergo an electrochemical reaction on the surface of the photocatalyst when the charges successfully migrate from the bulk to the surface (i.e., no recombination reaction). On the surface of the photocatalyst, the photogenerated electron and hole undergo water reduction and oxidation reactions, respectively. However, to facilitate (and accelerate) these reactions, another catalytic active site (cocatalyst) is introduced onto the surface of the photocatalyst. The presence of an efficient electrocatalyst as a cocatalyst is indispensable because each photon in visible light possesses a limited overpotential for water splitting. In addition, the cocatalyst will preferentially accommodate electrons (hydrogen evolution site) or holes (oxygen evolution site), preventing recombination reactions on the surface [7, 8, 18, 25–28].

From the mechanism for photocatalytic water splitting, it is clear that this reaction involves complex photophysical and chemical processes on different time scales. Our recent review addressed the fundamental parameters involved in photocatalytic overall water splitting [26]. The steps involved in the photocatalysis for water splitting are divided into the following six processes: (1) photon absorption, (2) exciton separation, (3) carrier diffusion, (4) carrier transport, (5) catalytic efficiency, and (6) mass transfer of reactants. All steps are illustrated in Fig. 1.

The current review aims to describe the relevant parameters related to the six processes mentioned above using Ta_3N_5 as a model photocatalyst. Some physicochemical properties, such as electronic structure, interface development, and electrocatalytic properties, will be described and correlated to achieve a comprehensive understanding of the complex sequential processes of overall water splitting.

Why Ta_3N_5?

For a semiconductor to be considered a good material for photocatalytic water splitting, there are several general requirements. First, to utilize visible light, it needs to have a low bandgap energy [7, 8, 18, 25–31]. A photocatalyst with a bandgap energy of approximately 2.1 eV, corresponding to a wavelength of 600 nm, is sufficient for achieving the targeted efficiency. The second requirement is that the photocatalyst band positions have to straddle the water redox potential ($E_{CB} > 0$ vs. RHE, $E_{VB} < 1.23$ vs. RHE) [7, 8, 18, 25–31]. Next, the photocatalyst needs to have excellent stability under the photocatalytic reaction conditions, under illumination and in the dark [7, 8, 18, 25–31]. Some potential low bandgap energy photocatalysts, such as CdS and CdSe, fulfill the first requirement and are very active for hydrogen evolution. However, these photocatalysts suffer from photocorrosion or self-oxidation due to their valence band positions, which lie more negative than the water oxidation potential [32–36]. WO_3, on the other hand, is very good for oxygen evolution, but its CB position lies more positive than the water reduction potential [37, 38]. Hence, compared to photoelectrochemical (PEC) systems, a single photocatalyst system has fewer choices of existing

photocatalysts. The fourth requirement is that the semiconductor should possess a high catalytic activity toward the oxidation or reduction of water. Finally, the semiconductor must be economically viable. Considering the scalability of the powder photocatalyst system, the photocatalyst must therefore be composed of inexpensive, abundant materials and have a largely scalable synthesis.

Studies on finding suitable and effective photocatalysts to fulfill all the aforementioned requirements have been conducted using various methods. Investigations have mainly focused on reducing the bandgap of the photocatalyst while maintaining its band position relative to the H^{+}/H_2 and O_2/H_2O redox potentials. The successful synthesis of a visible-light-responsive photocatalyst was demonstrated by the formation of (oxy)nitrides [19–24, 39–50]. Particular interest has been focused on Ta_3N_5 due to its absorption spectrum that can go up to 600 nm: a target for achieving efficient photocatalytic water splitting. It has been reported that Ta_3N_5 can generate H_2 or O_2 from water under visible light in the presence of suitable sacrificial reagents [19, 39–47].

Despite considerable studies as a photocatalyst for many years, information on Ta_3N_5 is still lacking regarding its thorough characterization to understand its underlying physical and chemical properties. Theoretical studies on this material are also limited. This review addresses the global picture of photocatalytic reactions using Ta_3N_5 as a model photocatalyst. This material was selected for two reasons. First, the initially reported photocatalytic activities were promising. Second, prior to the start of the work presented in this review, there were conflicting reports on the performance levels of different Ta_3N_5 materials, i.e., there was limited understanding of the factors that affect its photocatalytic performance.

Different methods for Ta_3N_5 synthesis

Ta_3N_5 is generally synthesized via the direct nitridation of crystalline tantalum oxide (Ta_2O_5) at high temperatures in the presence of NH_3 gas as a nitrogen source. The nitridation of tantalum oxide in a NH_3 flow proceeds in a complex manner, where the solid-state diffusion of anion replacements (N^{3-} vs. O^{2-}) occurs while gaseous NH_3 decomposes to nitrogen and hydrogen at high temperatures typically between 750 and 1150 °C [44, 51–54]. The process of anion diffusion requires the substitution of three oxygen atoms with two nitrogen atoms to maintain a high oxidation state of the Ta d^0 electronic configuration (Ta^{5+}). Depending on the amount of Ta_2O_5, the NH_3 flow rate and temperature are varied, typically in the range of 100–200 mL min^{-1} and 800–900 °C, respectively. This method generally produces sub-micrometer scale ($\sim$50–100 nm) Ta_3N_5 (Fig. 2a) with a low surface area ($\sim$10 m^2 g^{-1}). Ta_3N_5 powder has also been synthesized from amorphous Ta_2O_5, as reported by Henderson and Hector [55]. Using NH_3 gas between 680 and 900 °C, Ta_3N_5 with a crystal size of 20–30 nm was formed.

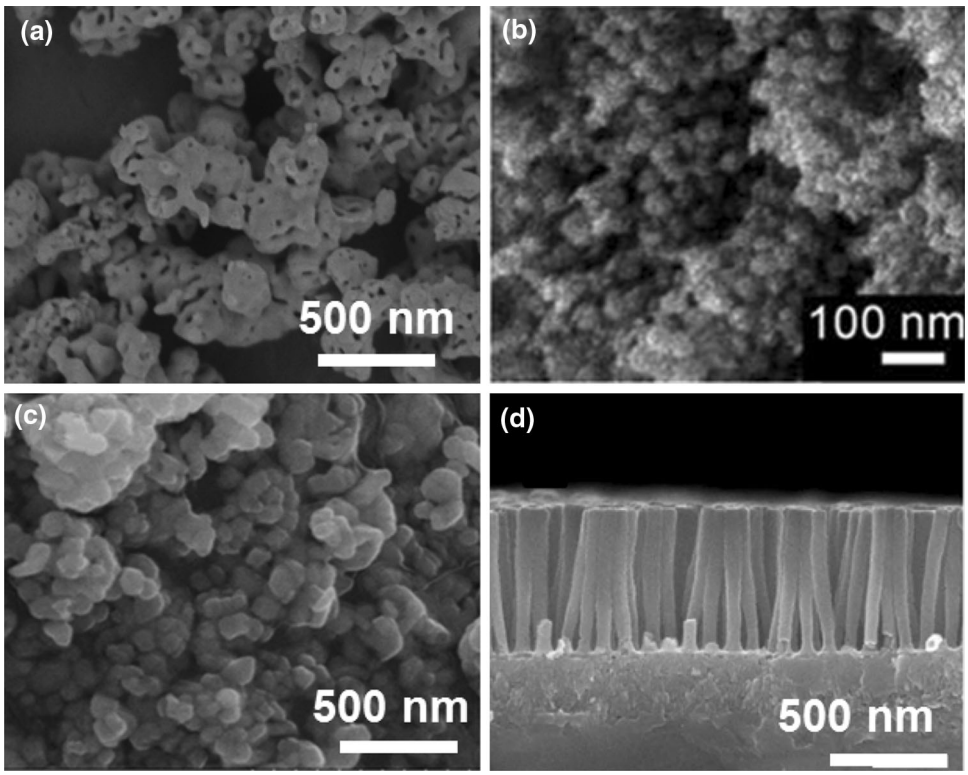

Fig. 2 SEM images of powder Ta_3N_5 synthesized with different method: **a** direct nitridation of Ta_2O_5, adapted from [44] with permission from the PCCP Owner Societies, **b** decomposition using mesoporous g-C_3N_4 template, adapted from [46] by permission of John Wiley & Sons Inc, **c** nitridation of Na_2CO_3-pretreated Ta_2O_5, adapted with permission from [42] Copyright (2012) American Chemical Society, and **d** nanorod Ba-Ta_3N_5 film synthesized by nitridation of Ta_2O_5 nanorods, adapted from [21] Copyright 2013, Nature Publishing Group

Direct nitridation generally produces Ta_3N_5 with good photocatalytic activity toward oxygen evolution but low activity for hydrogen evolution, approximately one order of magnitude lower than that for oxygen evolution [19, 39–47]. The resulting Ta_3N_5 generally contains some anion defects, as observed from its absorption spectrum after the band edge absorption ($\sim$710 nm), which is associated with its low photocatalytic performance due to the recombination reaction of photogenerated electrons-holes [43]. In addition, this method resulted in agglomerated Ta_3N_5 with a very low surface area [19, 39–47]. To overcome these problems, several attempts to improve the synthesis method of Ta_3N_5 have been pursued in various ways.

To improve the surface area and obtain a uniform size distribution, nanoparticle (NP) Ta_3N_5 has been successfully synthesized using mesoporous graphitic carbon nitride (mpg-C_3N_4) as a decomposable and reactive template [45, 46]. The particle size of Ta_3N_5 is controlled to sizes as small as approximately 7 nm by controlling (Fig. 2b) the pore size of the mpg-C_3N_4 template, and its surface area can reach 60 m^2 g^{-1}. The resulting Ta_3N_5 NPs exhibits improved photocatalytic activity for H_2 evolution in the presence of methanol as a sacrificial reagent. The size of semiconductor particles is believed to affect their photocatalytic activity by reducing the distance that the excited electrons and holes must travel to reach the active surface sites. Moreover, the size has also been hypothesized to affect the space-charge layer and band bending that govern the photocatalytic activity [45].

Improved photocatalytic hydrogen evolution was reported on Ta_3N_5 synthesized using a sol–gel method. In this method, Ta_2O_5 was first grown on the surface of SiO_2 spheres with a diameter of $\sim$550 nm and subsequently subjected to nitridation [47]. The final Ta_3N_5/SiO_2 sample exhibited a uniform size distribution with high crystallinity and a core–shell structure with a narrow size distribution without aggregation. The photocatalytic activity of the Ta_3N_5/SiO_2 samples toward hydrogen evolution was considerably higher than that of Ta_3N_5 synthesized via the conventional nitridation of commercial Ta_2O_5. Interestingly, when no SiO_2 was used, the photocatalytic hydrogen evolution of sol–gel Ta_3N_5 was relatively comparable to that of Ta_3N_5/SiO_2. Hence, attributing the improvement in photocatalytic activity toward hydrogen evolution to only the smaller particle size and higher surface area is questionable. Note that light scattering by SiO_2 in such a way to improve the absorption of light by Ta_3N_5 may occur. A simple physical mixture of SiO_2 and Ta_3N_5 did not improve photocatalytic performance; thus, an additional understanding of this type of supported photocatalyst is required.

Through a simple modification of the synthesis with an alkali metal salt, an improved photocatalytic oxygen evolution has been achieved on Ta_3N_5 [42]. In this method, the Ta_2O_5 precursor was first modified with an alkali metal salt (i.e., Na_2CO_3) prior to nitridation. This alkali metal salt produces a molten salt state at high synthesis temperatures (flux). The presence of the alkali metal salt improved the activity of Ta_3N_5 by affecting the crystal growth, which further led to higher crystallinity and a smaller particle size (Fig. 2c). Although low valence cation substitution may reduce the number of reduced Ta species by charge compensation, the enhanced physicochemical properties of Na-doped Ta_3N_5 and their relationship to higher photocatalytic activity remain unclear.

Quantum confinement in semiconductor nanoparticles (NPs) is believed to be capable of tuning the redox properties of the material if the size of the NPs becomes smaller than the exciton radius of an electron–hole pair [56, 57]. The synthesis of colloidal Ta_3N_5 NPs has been achieved by injecting a variety of reactive tantalum and nitrogen precursors into hot coordinating solvents under an inert atmosphere [58]. Through the use of different organic solvents and reaction times, the size of the NPs can be tuned in the range from 2 to 23 nm. A change in the bandgap energy of colloidal Ta_3N_5 NPs was observed from the absorption spectrum, where colloidal NPs have absorption onsets greater than that of the bulk powders by $\sim$0.3 eV. Despite the successful formation of very small Ta_3N_5 particles, this method suffers from very low Ta_3N_5 yields along with problems of Ta_3N_5 oxidation, which suggest that this method is not likely to be effective for the large-scale production of metal nitride nanoparticles [58].

The controllable synthesis of Ta_3N_5 with a tailored chemical composition and size has been attempted using urea as the N source rather than NH_3 gas [59]. By varying the urea/Ta ratio in the precursor gel, both TaON and Ta_3N_5 NPs with defined structures and sizes can be achieved. Assisted by SiO_2, the production of TaON and Ta_3N_5 NPs with tailored compositions was achieved through the calcination of Ta–urea gels with suitable urea/Ta ratios (RU/Ta). In this method, urea is first converted into carbon–nitride (CN_x) species on the surface of SiO_2 at mild temperatures, which further acts as a slow-release N source for controlled nitridation.

Regarding the synthesis of Ta_3N_5 electrodes, the majority of the films were obtained by Ta foil post-calcination [48, 49, 60], Ta anodization (Fig. 2d) [24, 61], or by sputtering [41, 62]. In our previous work on Ta_3N_5, we reported thin films with different thicknesses fabricated in a controlled manner using reactive direct current sputtering followed by optimal annealing and nitridation. The preparation of such Ta_3N_5 photoanodes in the form of dense thin films is a useful approach for obtaining a high crystalline quality that may effectively increase the efficiency of the process and the chemical stability of the PEC system. The thin film configuration also allows for thorough characterization of the photophysical properties of the

material, such as the Ta_3N_5 properties and photocatalytic performance.

Structural and optoelectronic properties of Ta_3N_5: detailed experiments and theoretical calculations

The crystal and electronic structures are two factors that primarily determine the absorption properties of a powder semiconductor [26]. The electronic properties of a semiconductor define the bandgap and band positions, the nature of direct and indirect light absorption, and the absorption coefficient. Essentially, the main effect resulting from direct and indirect bandgaps is the absorption coefficient, where a direct bandgap provides a high absorption coefficient and an indirect bandgap leads to a lower absorption coefficient. An indirect transition involves both a photon and a phonon because the band edges of the conduction and valence bands are widely separated in k-space. The crystal orbitals at the top of the valence band and at the bottom of the conduction band have the same wave vector in a direct bandgap solid but different wave vectors in an indirect bandgap material.

Crystal structure

The crystal structure of Ta_3N_5 was first reported by Brese and O'Keeffe using time-of-flight neutron diffraction [63]. Ta_3N_5 has an orthorhombic structure composed of irregular octahedra of N atoms with Ta atoms in the center. Two nitrogen atoms have four Ta atoms as the nearest neighbors, while another single nitrogen atom is coordinated to three Ta atoms. The Ta–N distances range from 1.96 to 2.24 Å and are similar to those in TaON.

The crystal structure of Ta_3N_5 based on our theoretical calculations is shown in Fig. 3a. Ta_3N_5 has an

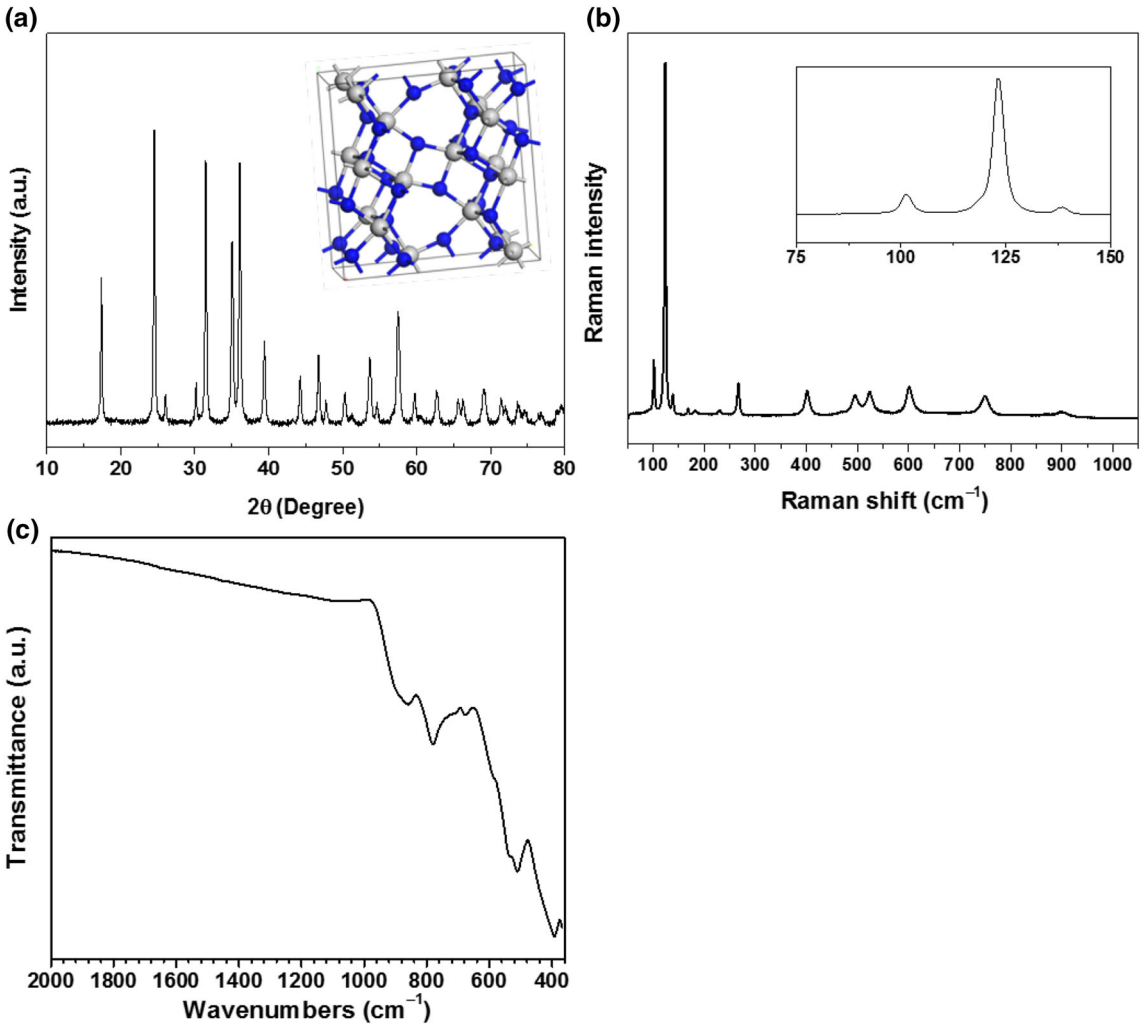

Fig. 3 **a** XRD pattern and crystal structure (*inset*), **b** Raman spectra, and **c** IR spectra of Ta_3N_5 obtained from nitridation of Ta_2O_5 by 15 h in NH_3 gas at 900 °C. Color legend for crystal structure: Ta in *gray* and N in *blue*. *All figures* are adapted from [64] by permission of Elsevier

orthorhombic structure with space group Cmcm, which is composed of edge-sharing irregular TaN_6 octahedra. Each Ta is coordinated by two N (that are threefold coordinated) and four N (that are fourfold coordinated) with Ta–N bond lengths ranging from 2.0 to 2.23 Å.

In our previous work, Ta_3N_5 powder was synthesized through the direct nitridation of crystalline Ta_2O_5 under a NH_3 flow at high temperature [43, 44, 64]. XRD characterization was performed to investigate the crystal structures of the synthesized materials. The successive nitridation completely changed the crystal structures of the products from the initial β-Ta_2O_5 to monoclinic β-TaON and then to orthorhombic Ta_3N_5, which is consistent with the literature [39, 40, 44]. The XRD patterns of samples heated at 800 and 900 °C for 15 h under different NH_3 flow rates were compared. For both temperatures, changing the flow rate clearly changed the TaON and Ta_3N_5 concentrations. At 900 °C, a mixture of oxynitride (TaON) and nitride (Ta_3N_5) material phases was observed for lower flow rates (i.e., 50-100 mL min^{-1} NH_3), whereas a higher amount of the Ta_3N_5 phase was observed at higher flow rates. Complete transformation of Ta_2O_5 to Ta_3N_5 was achieved after prolonged nitridation at 900 °C for 15 h under a 200 mL min^{-1} NH_3 flow. No remaining Ta_2O_5 or partially nitrided phase (e.g., β-TaON) was detected, as can be seen from XRD pattern presented in Fig. 3a. The resulting Ta_3N_5 has an orthorhombic crystal structure (ICSD card No. 1005006) with Cmcm space group. Similarly, for samples nitrided at 800 °C, the amount of the Ta_3N_5 phase increased with increasing NH_3 flow rate. However, at 800 °C, higher flow rates up to 500 cm^3 min^{-1} did not change the entire Ta_2O_5 precursor into the pure Ta_3N_5 phase. Some remaining TaON ($\sim$8 wt %) phase was still observed. It is suggested that competitive substitution of O with N between the NH_3 feed and H_2O occurred, where the chemical potential of oxygen kinetically determines these pseudo-thermodynamically stable phase diagrams [44].

The fact that a mixture of TaON and Ta_3N_5 always forms at 800 °C regardless of the flow rates under our conditions suggested that, during nitridation, the oxide was first transformed into oxynitride prior to nitride. This finding is in good agreement with reports in the literature, which state that TaON is the intermediate phase in the formation of Ta_3N_5 from the Ta_2O_5 precursor [39, 40, 51, 64]. This also implies that the nitridation proceeds via the successive transformation of Ta_2O_5 TaON Ta_3N_5, where a continuous dehydration reaction occurs. In this study, no concrete evidence could be found that the transformation of Ta_2O_5 to Ta_3N_5 is initially triggered by the incorporation of N atoms into the Ta_2O_5 lattice to form N-doped Ta_2O_5, as observed by Dabirian et al. where in situ XRD was utilized to follow the nitridation of Ta_2O_5 films [52].

The crystallite sizes for the synthesized samples and the lattice parameters were obtained from Rietveld analysis. The lattice parameters of Ta_3N_5 obtained from the XRD measurements and calculations are listed in Table 1. The calculated lattice parameters for Ta_3N_5 at the DFT/PBE level of theory are found to be in excellent agreement with the experimental data. The Ta_3N_5 samples synthesized at different temperatures with similar NH_3 flow rates and samples synthesized at 800 °C with different NH_3 flow rates did not exhibit any significant change in lattice parameters. Hence, the incorporation of N into Ta_2O_5 (i.e., the formation of doped-Ta_2O_5) is unlikely, as observed for the synthesis of Ta_3N_5 films [52]. In addition, the lattice parameters are also compared with those reported in the literature.

Lattice dynamics

Prior to our report, there was only limited literature on the lattice dynamics of Ta_3N_5 [43]. In our recent paper, detailed theoretical calculations and experimental results of Ta_3N_5 were explored [64]. Orthorhombic Ta_3N_5 with space group *Cmcm* is predicted to have a total of 24 Raman-active modes, $8A_g + 16B_g$, and 21 IR-active modes, $3A_u + 18B_u$. However, some frequencies predicted by the DFPT/PBE method have not been experimentally observed, most likely due to the low scattering cross-section of these modes and because the peaks are consequently hidden in the background. On the other hand, the experimental Raman spectrum exhibits 19 active modes and a few modes that are not predicted by the theoretical calculation. Nevertheless, the model generally reproduces the experimental data accurately, particularly at low wavenumbers.

The experimentally measured Raman spectra (Fig. 3b) show the most intense peaks at low wavenumbers, 102, 123, 138, 152, 168, 230, 266, 400, and 495 cm^{-1}, which are very well matched with the theoretically calculated peaks within 3–4 cm^{-1}. These modes are assigned to B_g, B_g, A_g, B_g, B_g,A_g, A_g, A_g, and B_g, respectively. However, at higher wavenumbers, the agreement is less evident. The experimental peaks located at 524 and 601 cm^{-1}, which are both assigned to A_g modes, are still quite well reproduced by the computed values within 5 cm^{-1}, whereas for the peaks at 749, 869, and 900 cm^{-1}, which are assigned to the B_g, B_g, and A_g modes, respectively, there is a larger variation in the range of 10 cm^{-1}. This behavior at higher wavenumbers was expected according to several reports in which the low energy part of the experimental spectrum was always better matched by theory than the higher energy part [71, 72]. Two peaks at 658 and 823 cm^{-1} were observed experimentally but not predicted by theory. These peaks were broadened and

Table 1 Comparison of Ta_3N_5 crystal structure obtained from theoretical calculation and experimental measurement

Crystal structure	Calculation	Experimental	Method/references
Lattice parameter			
a, b, c (Å)	3.89, 10.25, 10.27		DFT-PBE [44, 45, 65]
a, b, c (Å)		3.89, 10.22, 10.27	Powder XRD, Rietveld analysis [44, 45, 65]
a, b, c (Å)		3.89, 10.21, 10.26	Neutron diffraction [64]
a, b, c (Å)	3.87, 10.22, 10.26		PBE (QE) [68]
a, b, c (Å)	3.90, 10.33, 10.32		PBE (CRYSTAL) [68]
a, b, c (Å)	3.85, 10.14, 10.16		LDA (QE) [69]
a, b, c (Å)	3.99, 10.69, 10.69		rev PBE [70]
a, b, c (Å)	3.87, 10.24, 10.26		PBE [70]
a, b, c (Å)	3.91, 10.32, 10.35		PBE [71]
a, b, c (Å)	4.00, 10.43, 10.48		CGA + U [72]
a, b, c (Å)	3.87, 10.25, 10.27		HSE [71]
a, b, c (Å)		3.89, 10.22, 10.28	Neutron diffraction [56]
a, b, c (Å)			
Atom position			
Ta1 (4e); x, y, z	0, 0.198, 0.250	0, 0.197, 0.250	DFT-PBE and powder XRD, Rietveld analysis [65]
Ta2 (8e); x, y, z	0, 0.133, 0.559	0, 0.134, 0.560	
N1 (4e); x, y, z	0, 0.764, 0.250	0, 0.762, 0.250	
N2 (8e); x, y, z	0, 0.046, 0.120	0, 0.044, 0.116	
N3 (8e); x, y, z	0, 0.309, 0.073	0, 0.304, 0.072	
Ta1 (4c); x, y, z		0, 0.197, 0.250	Neutron diffraction [64]
Ta2 (8f); x, y, z		0, 0.135, 0.559	
N1 (4c); x, y, z		0, 0.763, 0.250	
N2 (8f); x, y, z		0, 0.047, 0.119	
N3 (8f); x, y, z		0, 0.309, 0.074	

enhanced in resonance conditions using $\lambda_{ex} = 532$ nm (2.33 eV) and $\lambda_{ex} = 473$ nm (2.62 eV), and likely due to LO overtones, were too weak to be observed in non-resonance conditions. In particular, the peak at 823 cm^{-1} observed with $\lambda_{ex} = 532$ nm might be the second overtone ($3\omega_{Ag}$) of $\omega_{Ag} = 266$ cm^{-1}, and the peak at 523 cm^{-1}, which was not very well matched by the theoretical models, might be the first overtone $2\omega_{Ag}$. In addition, these modes might also originate from different localized non-stoichiometries in the crystal that can be activated by one or various excitation wavelengths [44].

In addition to Raman's spectra, we reported calculated and experimentally measured IR spectra (Fig. 3c). There is a good agreement between the theoretical calculations with the experimental frequencies. However, most of the theoretically predicted modes cannot be associated with any experimental peak, probably because they are hidden in the background due to the low intensity. Moreover, a part of the spectrum, namely below 360 cm^{-1}, could not be measured experimentally due to the instrumental limitation.

Absorption coefficient and bandgap energy

The absorption spectrum of Ta_3N_5 powder is generally expressed from its diffuse reflectance spectrum [26]. Typically, Ta_3N_5 presents absorption from the UV region up to 600 nm, which is attributed to electron transitions from the N 2p orbitals to the empty Ta 5d orbitals [42]. The bandgap energy calculated using a Tauc plot (Fig. 4a, b) yielded values of 2.1 and 2.0 eV for the direct bandgap and indirect bandgap excitations, respectively; these values are in good agreement with previously reported values [18–29].

One interesting feature observed in the absorption spectrum of Ta_3N_5 is the extent of sub-bandgap absorption at approximately 715 nm. The enhanced sub-bandgap absorption at wavelengths greater than 600 nm has been previously assigned to reduced Ta^{5+}, which is presumably present at the surface of the Ta_3N_5 [62]. In contrast, Dabirian and Van de Krol [73] attributed the enhanced absorption of Ta_3N_5 at wavelengths greater than 600 nm to its bulk properties rather than to its surface. The highly charged nitrogen vacancy that formed during prolonged

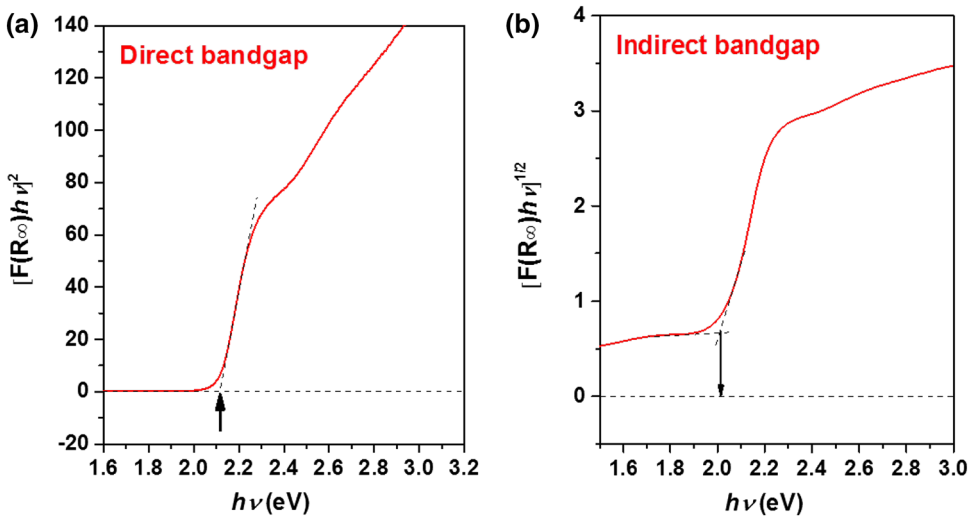

Fig. 4 Tauc's plots of Ta_3N_5 for **a** direct and **b** indirect bandgaps. *Figures* are reproduced from [64] by permission of Elsevier

nitridation is a likely candidate for the deep donor state responsible for the absorption feature at wavelengths greater than 600 nm. This assignment was rationalized by the fact that oxygen is always present at the 3-coordinated nitrogen sites in the Ta_3N_5 structure. To elaborate the origin of this sub-bandgap absorption, a theoretical calculation was performed [43]. The 720 nm sub-bandgap optical absorption of Ta_3N_5 was formed due the appearance of new deep donor metallic states located within the 0.7 eV range just below the original conduction band edge of pure Ta_3N_5, which corresponds to reduced Ta species (Ta^{3+}) originating from O species substituted at N sites, as in $Ta_3N_{4.83}O_{0.17}$. This finding is in a good agreement with the Raman spectra, where the Ta_3N_5 crystal is most likely non-stoichiometric with oxygen substituted for nitrogen [64]. Indeed, elemental analysis under a control atmosphere always shows the presence of oxygen even though XRD shows a pure phase of Ta_3N_5 [43, 44, 64]. In line with this, our group has systematically investigated the possible structures and found that the experimentally prepared tantalum nitride materials are most likely not stoichiometric but strongly enriched in O, closer to $Ta_{(3-x)}N_{(5-5x)}O_{5x}$ (for $x \geq 0.16$) rather than Ta_3N_5 [44].

We can accurately deduce the Ta_3N_5 absorption coefficient from the transmittances and reflectances of different thicknesses of thin films. An absorbance edge of ~600 nm was observed for all of the films, which is consistent with the reported 2.1 eV bandgap of Ta_3N_5 [30]. As can be seen in Fig. 5a, the absorption coefficient appears to monotonically decrease with increasing wavelengths, and the values are relatively low, starting from 8×10^5 to 1×10^4 cm^{-1} in the spectral range relevant to the PEC measurement (300–600 nm). In addition to absorption coefficient measurements from Ta_3N_5 thin films, we performed theoretical calculations of the absorption coefficient [44, 64]. In agreement with those reported in the literature, in our calculations for pure Ta_3N_5, the density of states (DOS) calculated using the HSE06 functional predicts a bandgap of 2.2 eV (Fig. 5c). The electronic analysis reveals a VB governed by occupied N 2p states and a CB that is primarily composed of empty Ta 5d states. Our bandgap of 2.2 eV calculated using HSE06 closely matches the available experimental data. Based on the DOS results, our UV–Visible optical absorption spectrum calculated using DFPT-HSE06 reveals a broad absorption edge extending to 564 nm (Fig. 5b). The lowest-energy bandgap in this compound involves transitions between N $2p^6$ orbitals and Ta $5d^0$ orbitals. Similar absorption behavior was exhibited by non-stoichiometric Ta_3N_5 (O-enriched Ta_3N_5) materials. The lowest-energy bandgaps in these compounds involve transitions between N $2p^6$ orbitals and Ta $5d^0$ orbitals. Their calculated UV–Vis optical absorption coefficient spectra are found to be slightly blue-shifted over pure Ta_3N_5, revealing new absorption onsets at 540, 517, and 497 nm, respectively (Fig. 3b). The top part of the valence band in these compounds is dominated by occupied N 2p states due to the very weak contributions from O 2p states distributed over a wide energy range in the deeper part of the valence band, which caused the shifting of the absorption spectra.

Direct/indirect bandgap nature

The DOS of Ta_3N_5 was calculated to understand the nature of direct/indirect bandgaps [43, 44, 64]. Our calculated DOS is presented in Fig. 5c, in which the valence band is dominated by completely filled N 2p states and the conduction band is primarily composed of Ta 5d states. This compound can be identified as a direct (at the Γ or Y point) or an indirect (Γ-Y) semiconductor with the same bandgap energy of 2.2 eV. Inconsistent with our work, a previous

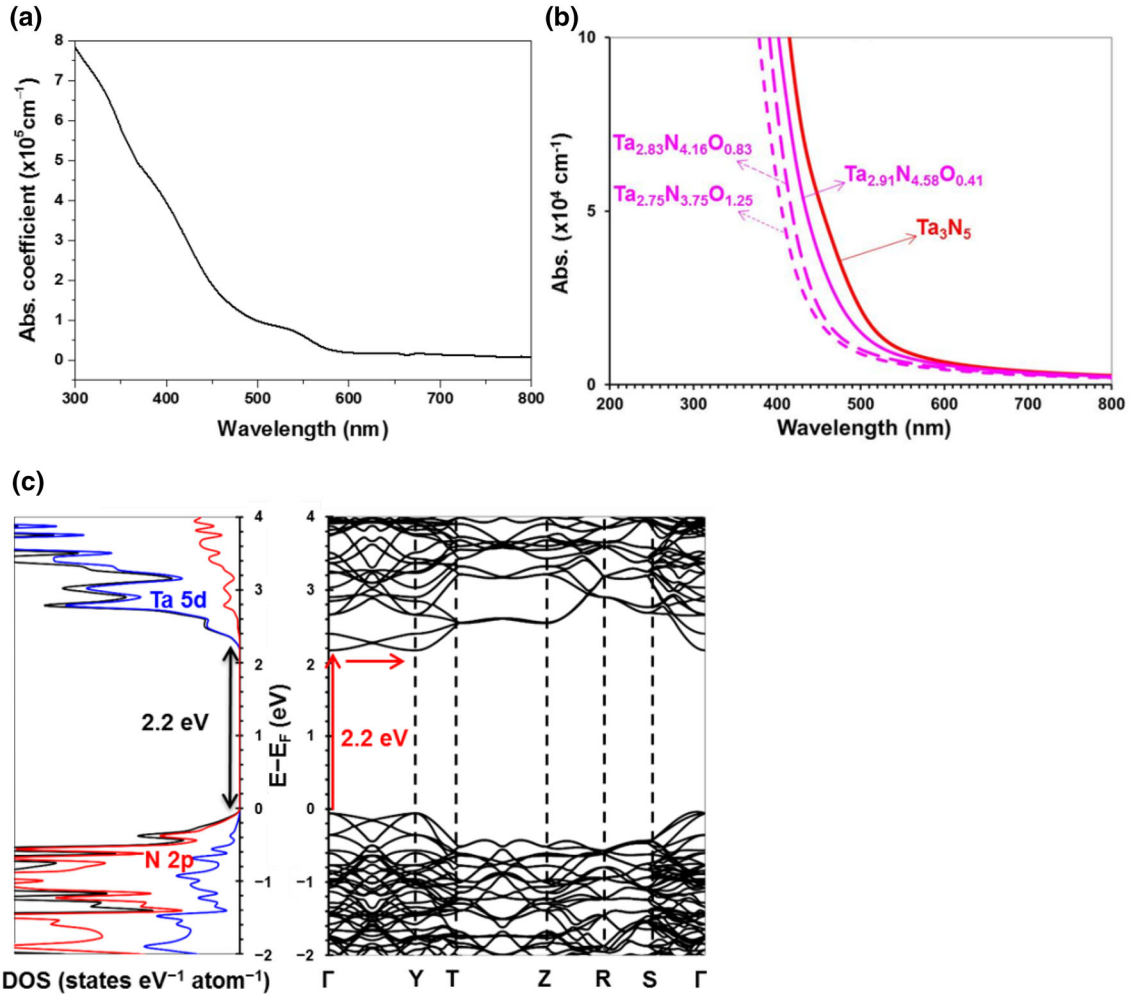

Fig. 5 Absorption coefficient **a** obtained from experimental measurement, adapted from [41] with permission from the PCCP Owner Societies and **b** obtained from theoretical calculation, adapted from [44] with permission from the PCCP Owner Societies, and **c** electronic density of states (DOS) and *k*-space band structure diagrams computed at the DFT/HSE06 level of theory for Ta_3N_5. Color legend: total DOS (*black*) and the partial contributions from Ta 5d orbitals (*blue*) and N 2p orbitals (*red*). Fermi level is set at 0 eV, adapted from [64] by permission of Elsevier

study on calculating the DOS of Ta_3N_5 has shown that it is an indirect bandgap semiconductor with the VBM located at the Γ point and the CBM located at the Y point. The density of states shows that the top of the valence band is primarily composed of N 2p orbitals, whereas the bottom of the conduction band is mainly composed of Ta 5d orbitals.

In addition to the DOS calculation and DR–UV–Vis absorption, we studied the photoluminescence (PL) spectra of Ta_3N_5 to investigate its absorption properties [64]. The photoluminescence spectra of Ta_3N_5 were acquired using 473 and 532 nm lasers as excitation sources. Ta_3N_5 has a quite narrow PL centered at 580 nm that is considerably more intense when $\lambda_{ex} = 532$ nm is used. This PL is related to the direct bandgap transition at the Γ point (2.2 eV) with slightly lower energy for the absorption onset due to non-radiative recombination.

Band position

The flatband potentials of Ta_3N_5 are typically estimated from Mott-Schottky experiments or ultraviolet photoemission spectroscopy (UPS) measurements [19]. The first study on Ta_3N_5 flatband potentials was reported by Chun et al. utilizing Mott-Schottky and UPS measurements [19]. Both techniques provided good agreement with a flatband potential of −4.44 eV (0 V vs. NHE at pH = 0). Another work by Cong et al. [24] found the flatband potential of Ta_3N_5 to be −0.05 V vs. NHE (pH = 0).

In our work, we utilized a Mott-Schottky experiment to estimate the Ta_3N_5 flatband potential [43, 44]. The Mott-Schottky analysis at pH 13.5 provided a flatband potential of ∼−0.5 V vs. RHE. The experimentally obtained flatband potential is considered to be located close to the conduction band and is consistent with the fact that the

contribution of conduction bands is commonly strongly associated with empty Ta d^0 orbitals for Ta_3N_5. Here, the band positions are assumed to follow a typical pH dependence relationship of 0.059 × pH (in V) such that the band positions relative to water redox potentials remain constant at any pH [19]. In addition, the slope of the Mott-Schottky graph exhibited a positive value, characteristic of n-type semiconductors. From the bandgap obtained from the measurement of optical properties, the measured conduction and valence band positions are located at ~ -0.5 and 1.6 V vs. SHE (at pH 0). Based on these data, the band positions for Ta_3N_5 are suitably located for overall water splitting (they straddle the water redox potentials).

The band positions of Ta_3N_5 were predicted through theoretical calculations [44]. For pure Ta_3N_5, the HSE06 calculations predict the VB edge position to be 0.3 eV higher in energy than the O_2/H_2O level. The CB edge position is found to be 1.3 eV higher in energy than the H^+/H_2 level. Because of its unsuitable VB edge position with respect to the O_2/H_2O potential, pure Ta_3N_5 is predicted to be a good candidate only for the hydrogen evolution reaction. It is important to discuss here the potential error bars in the calculation of the band edge positions. General benchmarks are available for the ionization potential and electron affinities of molecular sets, and they indicate a mean absolute error of ~ 0.2 eV. Regardless, the VB edge position is not below the O_2/H_2O level, and thus, the holes created upon photon absorption in pure Ta_3N_5 will have a very limited (if not null) capability to oxidize water. Additionally, the pH value is able to slightly affect the O_2/H_2O potential. In contrast, the position of the CB band edge is undoubtedly above the H^+/H_2 level, and the excited electrons thus have a strong capability to reduce H^+.

The predicted band edge positions for pure Ta_3N_5 are found to differ from the experimental results. For the experimental results, the measurements and calculations are based on the Mott-Schottky relationship, where the surface states may present and play a crucial rule in modifying the band positions [19, 24, 43, 44]. This effect, however, was not taken into account for the theoretical calculations. In addition, as mentioned previously, the formation of pure Ta_3N_5 is not possible. Although the XRD patterns show the pure phase, the elemental analysis shows a considerable amount of remaining oxygen for Ta_3N_5, which indicates an oxygen-enriched Ta_3N_5 crystal structure. Our group has systematically predicted the band edge positions of various oxygen-rich Ta_3N_5 structures through theoretical calculations. The measured band edge positions are found to be highly consistent with the band edge positions for O-enriched Ta_3N_5 materials, particularly for the non-stoichiometric $Ta_{(3-x)}N_{(5-5x)}O_{5x}$ (for $x \geq 0.16$) compounds. Considering the accuracy of bandgap prediction using the HSE06 functional, this result confirms that the experimentally prepared tantalum nitride materials are not stoichiometric but rather strongly enriched in O, as also observed from Raman and DR-UV–Vis absorption spectra.

The optical properties and band positions based on our experimental results and calculations and those reported in the literature are compared in Table 2.

Kinetic and dynamic properties of photoexcited carriers on Ta_3N_5

Charge carrier separation

In photocatalytic reactions, it is important to examine the separation of charge carriers in the photocatalyst. The dielectric constant is an important parameter that describes the interaction of the electric field with the material's medium. As defined by many researchers [66, 67, 76, 79–83, 84], the extraction of charge is greatly dependent on the material's dielectric constant. In general, a high dielectric constant (10 or more) was found to induce good exciton dissociation into free charge carriers. Furthermore, knowing the dielectric constant allows the donor density of the material to be calculated, which is an important parameter for describing the intrinsic nature of semiconductors. In general, the dielectric constant is dependent on the different vibrational modes induced by time scale variations. At low frequency, there is only an ionic contribution called the vibrational dielectric constant (ε_{vib}). At high frequency, there is an additional contribution coming from the electronic vibrational mode (ε_∞). For Ta_3N_5, ε_{vib} is almost used as 110 [21]. We calculated the imaginary part of the frequency-dependent dielectric function over the three principal light polarization vectors as a function of the photon energy using the DFPT/HSE06 method, and the obtained spectra are displayed in Fig. 6a [64]. High dielectric constants of 35.15, 39.68, and 53.88 were obtained along the principal crystallographic directions with an average value of 43. For the electronic dielectric constant contribution, it was calculated using density functional perturbation theory at the DFT/PBE level of theory and at the experimental geometry, as well as by employing the QE code. It was found to be between 8 and 11.5 [67, 70, 77].

In our previous work, we reported the measurement of the dielectric constant of Ta_3N_5 films from the fringes observed in the transmittance and/or reflectance spectra [41]. The details of the measurements and calculations were also described. The dielectric constants for different film thicknesses are presented in Table 3. Experimentally, to estimate the electronic vibration of the dielectric constant, we use the complex index of refraction $N = n + ik$. From the fringes observed in the transmittance and/or reflectance spectra, we can deduce the dielectric constant

Table 2 Ta_3N_5 optical properties and band positions

Optical properties	Calculation	Experimental	Method/references
Bandgap energy (eV)			
		2.1	DR-UV–Vis [19–21, 40–48]
		2.1	UV–Vis [41, 100]
	2.20^{D}		DFT-HSE06 [44, 64]
	2.20^{I}		DFT-HSE06 [64]
	1.43^{I}		PBE [67]
	1.88^{I}		PBE [67]
	2.12^{D}		Sc-hybrid [67]
	2.90^{I}		PBE0 [70]
	2.20^{I}		HSE [69]
Flatband potential (V vs. NHE)			
		0 (pH 0)	Mott-Schottky [19]
		−0.02	UPS [19]
		−0.05 (pH 0)	Mott-Schottky [24]
		−0.3 (pH 13)	Mott Schottky [41, 43, 44]
Conduction band			
		−0.3 (pH 0)	Mott-Schottky [19]
		−0.52 (pH 0)	UPS [19]
	−1.3 (pH 0)		HSE06 [74]
	−0.4 (pH 0, defective Ta_3N_5)		HSE06 [74]
Valence band			
		+1.58 (pH 0)	Mott-Schottky [19]
		+1.58 (pH 0)	UPS [19]
	+0.9 (pH 0)		HSE06 [74]
	+1.6 (pH 0, defective Ta_3N_5)		HSE06 [74]
Absorption coefficient (cm^{-1})			
	1×10^5		HSE06 [44, 64]
		8×10^5–1×10^4	UV-Vis spectroscopy [41]
		6.2×10^4	UV-Vis spectroscopy [60]
		2.5×10^5–3×10^3	Spectroscopic ellipsometry [75]
	1.4×10^5–2.2×10^5		BSE-G_0W_0 [67]

D direct bandgap, *I* indirect bandgap

$\varepsilon_1 = n^2 - k^2 \approx n^2$ (for low absorption) and $\varepsilon_2 = 2nk$. Thus, the obtained dielectric constants were approximately 12.5 and 13 in the visible spectral range for Ta_3N_5-160 nm and Ta_3N_5-470 nm, respectively [26, 41]. Because of the very thin thickness of the Ta_3N_5-50 nm sample, there were no fringes observed. Therefore, we can use another formalism to extract dielectric constant. We calculated the dielectric constant from a calculation of the real part of the index of refraction from the reflectance and transmittance measurements [78]. The real part of the dielectric constant is linearly related to the wavelength in the non-absorbing region [78]. Figure 6b shows the plot of ε_1 vs. λ^2 for the Ta_3N_5-50 nm thin films. The intersection of the linear part of this curve provides the value of the dielectric constant, and the N/m* ratio can be calculated from the slope of the straight line. From this extrapolation, we determined the dielectric constant to be equal to 13.8. Moreover, we can estimate the relative mass of the material. Indeed, relative mass is another important parameter that can provide an idea about the charge diffusion in the photocatalyst. It will be developed in the following section.

Clearly, there is a significant difference among the measured and theoretically calculated dielectric constants [41, 64]. For the measured dielectric constant, the experiment was conducted only for high frequency (UV–Vis range), where it contributes only to electronic vibration, whereas for the calculated dielectric constant, both low and high frequencies were taken into account, and therefore, the dielectric constant also considered the ionic and electronic contributions [41, 64, 66].

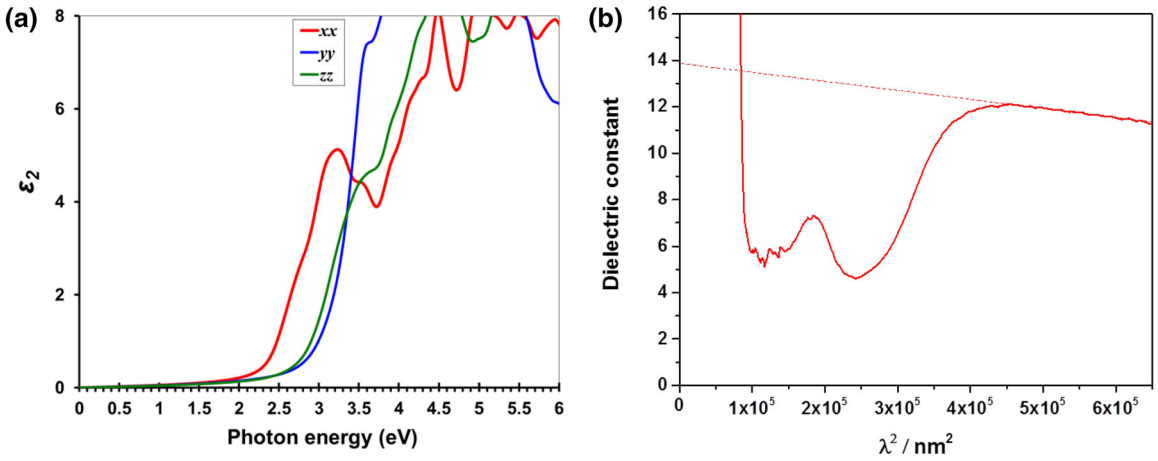

Fig. 6 **a** Imaginary part of the frequency-dependent dielectric function along with the three principal light polarization vectors computed at the DFPT/HSE06 level of theory for Ta_3N_5 utilized for dielectric constant calculation. *Red*, *blue*, and *green curves* correspond to *xx*, *yy*, and *zz* components, respectively, adapted from [64] by permission of Elsevier and **b** *plot* of the dielectric constant vs. λ^2 of Ta_3N_5 thin film for electron effective mass determination

Table 3 Ta_3N_5 kinetic and dynamic properties

Kinetic and dynamic properties	Calculation	Experimental	Method/references
Dielectric constant[a]			
	43		LR-DFPT-PBE [64]
		17[b]	Reflectance fringe [41]
		110	Not specified [21]
		7–9	Spectroscopic ellipsometry [75]
	65		PBE [67]
Electron Effective mass[c]			
	0.60 m_0–1.94 m_0		FD-DFT-HSE06 [64]
	0.23 m_0–2.70 m_0		DFT-PBE [67]
		0.36 m_0	Reflectance measurement [40, 41]
Hole Effective mass[c]			
	0.85 m_0–3.38 m_0		FD-DFT-HSE06 [64]
	0.66 m_0–3.56 m_0		DFT-PBE [67]
Charge carrier concentration (cm^{-3})			
		5×10^{17}–5×10^{20}	Hall effect measurement [41]
		3.7×10^{19}	Mott-Schottky plot [21]
Mobility ($cm^2\ V^{-1}\ s^{-1}$)			
		1.3–4.4	Van der Pauw [41]
Carrier lifetime (ps)			
		3–9	Transient spectroscopy [41]
		2–12	Femtosecond DR-spectroscopy [86]
Diffusion length (nm)			
		3–9	Subtracted from mobility and lifetime [41]

A average value for different crystal orientations, calculated as the total dielectric constant considering ionic and electronic contributions (i.e., low and high frequencies), *b* measured only for high frequency (electronic contribution), *c* depending on crystal orientation

Charge carrier diffusion

Quantitatively, charge carrier diffusion can be examined from the effective mass property. Acceptable effective masses are considered optimal, at least in one crystallographic direction, when they are less than 0.5 m_0 (m_0 being the electron mass) for an efficient diffusion of charge carriers in the material [64, 66, 79–83]. For a measured

donor density of 5×10^{20} cm^{-3}, deduced from Mott–Schottky measurements, we estimate the electron effective mass to be 0.36 m_e^* for Ta_3N_5-50 nm using Fig. 6b. We also computed the charge carrier effective masses (i.e., electron and hole effective masses) and compared them to previous experimental works on semiconductors used in photovoltaic devices. The smallest hole and electron effective masses are both found to be along either the [001] or [010] direction with $m_h^* = 0.85\ m_0$ and $m_e^* = 0.6\ m_0$, and the highest hole and electron mobilities are expected to be along these two specific directions. These two obtained values are larger than 0.5 m_0 (threshold value), and hence, relatively poor charge carrier transport properties are expected along this specific direction. Note that the current data using the DFT/HSE06 level of theory had a subtle discrepancy with the reported values using the DFT/PBE level of theory [85], as expected from the different calculated energy diagrams. In addition, compared to the calculated electron effective mass obtained from measurements, 0.36 m_0, the value is below the threshold, and thus, good electron charge carrier transport is expected. Calculations estimate the electron effective masses to be between (0.2–2.7 m_e^*) [64, 67] depending on the crystallographic direction. Additionally, it appears that the effective masses of holes are larger than those for electrons (0.66–3.6 m_h^*). This result suggests that low hole mobility may be responsible for the limitation of the generated photocurrent in Ta_3N_5.

The charge carrier concentration can be calculated from the slopes of the Mott-Schottky plots. Using a geometric area of the films, the obtained values were $\sim 5 \times 10^{19}$ cm^{-3} for the thin films and 5×10^{20} cm^{-3} for the thicker ones. If the relative surface area of the thicker film was used, the carrier concentration of this film was in the same range as the rest of the samples. Clearly, the donor density measurement from the Mott-Schottky analysis is very complex; therefore, the carrier concentrations of the films were also measured using Hall measurements. We found values between 5×10^{17} and 5×10^{20} cm^{-3}, which are within the same range for other reported photoanodes, such as hematite or bismuth vanadate materials [103–105]. We also reported on the electronic transport properties (carrier mobility) and spectroscopic measurements (carrier recombination). These two parameters determine the diffusion length of the material and can be correlated to the PEC performances. The van der Pauw four-probe measurement provides the resistivity of the material, and the Hall measurements provide the charge carrier concentration. The resistivity of the films decreased from 32.44 to 0.01 O cm with a thickness increase from 160 to 470 nm, which correlates to the crystallinity of the films. For the thick films (960 nm), the resistivity increased to 54.88 O cm. All of these values are within the range of typical semiconductor materials (10^{-3} – 10^{3} Ω cm). The calculated mobilities were in the range of 1.3–4.4 cm^2 - V^{-1} s^{-1}. Thicker films possess better mobility.

The intrinsic defects in Ta_3N_5 can significantly reduce the carrier lifetime and consequently decrease the photocurrent. It is well known that the carrier lifetime is significantly increased by enhancing the film morphology, grain size, and crystallinity. Femtosecond (fs) transient absorption spectroscopy provides direct information regarding the carrier dynamics and excited-state deactivation pathways, including carrier trapping. We utilized this method to probe the events that occurred due to photoexcitation of the Ta_3N_5 films. We explored the carrier dynamics of Ta_3N_5 thin films using broadband transient absorption spectroscopy with 120 fs temporal resolution. We observed a significant increase in the carrier lifetime of the thick films compared with the thinner films. The observed dynamics can be attributed to the decrease in carrier trapping, indicating that there are less defects in the thicker film compared with the thinner one, consistent with the crystalline structure and the surface morphology of the thick films. The measured lifetimes are in the range of 3.1–8.7 ps, consistent with the 12 ps reported for Ta_3N_5 powder [86]. Using the mobility and lifetime, we can estimate the Ta_3N_5 diffusion length to be between 3 and 9 nm, which again highlights the difficulty in diffusing charge carriers. Material structuration and cocatalyst addition are mandatory to diffuse charge carriers and subsequently improve the photocatalytic reaction.

The kinetic and dynamic properties from our experimental and theoretical calculation results and those reported in the literature are compared in Table 3.

Ta_3N_5-electrolyte interface

Surface states related phenomena

The photocatalytic activity of Ta_3N_5 for oxygen and hydrogen evolution reactions has primarily been attributed to its activity related to its bulk properties, such as crystallinity, particle size, and optical properties [18–20, 22, 23, 26, 29, 30]. However, as previously described, photocatalytic water splitting is a complex reaction that is affected by many factors associated with the photocatalyst and cocatalyst properties. Although the effect of the surface properties of semiconductors is significant, it is less investigated and correlated with photocatalytic activity.

Our work reported that not only the bulk properties but also the surface properties greatly affected the photocatalytic activity of Ta_3N_5 [43]. A thin TaN layer on the surface ($\sim$2 nm), which formed depending on the synthesis method, was observed to change the energetic profile

on the Ta_3N_5-electrolyte interface, thus changing the photocatalytic activity. The surface layer changes the potential distribution on the Ta_3N_5 surface-electrolyte interface, as evidenced by the perturbed flatband potential. The flatband potentials shifted as a consequence of Fermi level pinning of the semiconductor-electrolyte interface due to the drastic influence of surface states. However, the surface states were difficult to elucidate in this study, but it can be said that the layer, which can be removed by alkaline piranha solution, shifted the overall flatband potential to be more negative without changing the bandgap, consistent with the enhanced hydrogen evolution while minimizing the oxygen evolution. This study also emphasized the importance of surface modification to improve the photocatalytic performance. Interface modification together with cocatalyst function and intentional perturbation of the surface states by introducing an additional hetero-layer would have the potential to further improve the photocatalytic performance.

Mott-Schottky analysis

One of the requirements of a photocatalyst to undergo photocatalytic/PEC reactions is possessing suitable band positions with respect to the water redox potentials (thermodynamic requirement). To estimate the band positions, Mott-Schottky plots using impedance spectroscopy were obtained in an attempt to retrieve the flatband potential [26, 41]. Note that the Mott–Schottky relation is only applicable to "ideal" semiconductors with a uniform bulk and surface and with preferably known surface areas. Additionally, the surface states present on the semiconductor significantly affect the Mott–Schottky plot because the pH effects follow the Nernstian relationship of -59 mV pH^{-1} for many semiconductors. Hence, the fabrication of high-quality electrodes using powder semiconductors is indispensable for obtaining reliable results [26, 41].

Several works have reported the flatband potentials of Ta_3N_5 films synthesized using different methods, where the reported flatband potentials show different values for different film preparations [19, 24, 41]. In addition to films synthesized from Ta_3N_5 by applying electrophoretic deposition, we applied the sputtering method to synthesize Ta_3N_5 on Ta foils with different thicknesses [41, 43, 44]. The Mott-Schottky plots for the Ta_3N_5 films with different thicknesses were determined based on the impedance data. All of the Ta_3N_5 films exhibited positive slopes, which are characteristic of n-type semiconductors.

To obtain accurate flatband potentials, the selection of a suitable potential window for extrapolation from the Mott-Schottky plots is crucial. For this purpose, the Faradaic current should remain negligible. However, in most cases, the non-flat behavior of the capacitive current causes difficulty in selecting the right potential window for measuring the flatband potential. For example, in our case, in the potential range from -1.2 to $+1.0$ V vs. RHE, the Mott-Schottky analysis leads to a flatband potential from -0.1 to 0 V vs. RHE, which is consistent with previously reported values. However, in a different potential range at more positive potentials, the flatband potential can be found between $+0.8$ and $+1.1$ V vs. RHE, which are more positive compared with those reported. Notably, the flatband potentials mentioned in the literature were taken in different potential ranges, resulting in different flatband potentials. Mott-Schottky analysis is more preferable for studying the flatband potential of a single-crystal semiconductor with a moderate doping content and a good ohmic contact [26, 41, 87]. These ideal conditions are not the case for these samples nor those reported in the literature. Additionally, due to the surface state capacitance and associated double-layer capacitance at the semiconductor-electrolyte interface, it is often observed that the flatband potential depends on the frequency used, which should not be the case.

Upon successful charge transfer, the culmination of all the photophysical processes on the semiconductor surface succeeds with an effective electrocatalytic process [1, 26, 88]. An efficient electrocatalyst is one of the most important parameters for achieving efficient photocatalytic water splitting in visible light. To achieve efficient water splitting under visible light irradiation where there is no significant overpotential for electrocatalysis, the electrocatalysts need to transfer the received electrons and holes to the relevant reactants in the water splitting redox reactions [1, 26].

OER cocatalyst deposition effect on Ta_3N_5

A comprehensive understanding of the cocatalyst and of its fundamental effect on photocatalytic water splitting has yet to be elucidated. Studies on electrochemical water splitting have obtained some promising results regarding the development of oxygen evolution reaction (OER) cocatalysts. Some new cocatalysts, such as Co_3O_4, $Ni(OH)_2$, and Mn_3O_4, have good potential for replacing the employed noble metal catalysts (RuO_2) because of their excellent electrocatalytic activity [76, 87–90]. However, little attention has been focused on investigating these materials as OER cocatalysts in photocatalytic water splitting. Despite the difference in these two systems, this electrochemical approach is applicable for studying the surface reaction of water oxidation.

Physical and chemical properties of CoO_x on Ta_3N_5 surface

Cobalt oxide (CoO_x) has been extensively investigated as a cocatalyst, particularly for electrochemical and PEC OER [15, 24, 91–98]. Although many studies have reported improvement of the electrochemical OER using CoO_x, studies on powder suspension systems are limited [42, 93]. An improved photocatalytic OER rate with a quantum efficiency as high as 27 % (at 440 nm) has been reported on $LaTiO_2N$ with deposited CoO_x [93]. In addition to providing active sites for the electrocatalytic OER, CoO_x is also believed to play a vital role in promoting charge separation. However, despite the tremendous efforts toward developing a CoO_x catalyst, its chemical state and properties on a photocatalyst have yet to be elucidated.

In our recent work, quantum efficiencies as high as 19.4 % (at 440 nm) were achieved on CoOx/Ta_3N_5 in the presence of $AgNO_3$ as a sacrificial electron acceptor [99]. The effect of CoO_x addition and heat treatment on the photocatalytic OER on Ta_3N_5 was investigated based on the photocatalytic OER performance and thorough characterization. Nitridation after Co impregnation essentially creates a metallic cobalt–cobalt oxide core shell structure with intimate contact between the Ta_3N_5 surface and the cocatalyst, as indicated by STEM image depicted in Fig. 7a, b.

This intimate contact led to drastic improvements in the photocatalytic efficiency for the OER. This state is also consistent with the results obtained by Raman, XAS, and XPS measurements. However, the metallic state of cobalt is not an essential component of the improved OER because it disappeared after the photocatalytic reaction. The high-temperature treatment is likely to form an intimate contact between the Ta_3N_5 surface and CoO_x, facilitating effective hole transfer. Subsequent mild oxidation led to further improvement of the photocatalytic OER, indicating that CoO_x is a preferred active site for the OER over the metallic phase. The photocatalytic OER activity using Ta_3N_5 as photocatalyst from our study and that reported in literature are compared in Fig. 8a, b.

Kinetics and dynamics of photoexcited carriers on CoO_x/Ta_3N_5 and noble metal co-loaded CoO_x/Ta_3N_5

The effect of cocatalyst modification on improved photocatalytic/PEC performance has been a matter of debate. The role of the cocatalyst has been reported to provide two effects: 1) improvement in electrochemical performance by lowering the overpotentials for the redox reactions, and 2) effectively separating the excited charges utilizing the photocatalyst (semiconductor)–catalyst interface through the differences in Fermi levels between them.

In a previous work, a substantial improvement of the electrocatalytic OER was observed when Au was added to the CoO_x electrode [91]. The beneficial effects of the two coexisting metals were speculated to be increasing the population of Co^{IV}, which are believed to be the active sites for the OER. Knowing that CoO_x is a more preferable active site for the photocatalytic OER, we attempted to improve the OER rate by simply adding a trace amount ($\sim$0.05 wt %) of noble metals to a cobalt-modified Ta_3N_5. The photocatalytic OER over Pt or Ir co-loaded CoO_x/Ta_3N_5 is presented in Fig. 9.

The optimized system exhibited one of the highest quantum efficiencies (QEs) reported over 20 % in visible light range in 0.1 M $Na_2S_2O_8$ at pH 14. Using time-resolved spectroscopy, we are attempting to identify whether hole transfer kinetics is improved by the addition of noble metal. The initial attempts likely suggest that hole transfer was also improved, and the results are to be published in the near future. In addition, as claimed in the literature, improved electrocatalytic OER by lowering the onset potential also plays a significant role in enhancing the photocatalytic OER [90].

As previously mentioned, investigating electrocatalysis is one of the best approaches for studying photocatalytic water splitting. In our recent review, we included the mass transfer of reactants, which significantly affects the photocatalytic water splitting performance [26]. The study of photocatalytic water splitting has primarily focused on developing efficient materials, including cocatalysts, without consideration of thermodynamic and kinetic information from the electrocatalysis perspective. Indeed, in a single powder photocatalyst system, there is no pH gradient because the H_2 and O_2 are generated in the same compartment.

Most of the photocatalytic water splitting is conducted at neutral pH due to the stability issue of most semiconductor photocatalysts. Therefore, it is important to study the electrolysis of water under neutral pH. In acidic or alkaline conditions, pH 0 and 14, respectively, one H^+ or OH^- ion is present among approximately 55 H_2O molecules. In terms of kinetics, the reaction with hydronium ions (protons) or hydroxyl ions that have a very large diffusion coefficient is more facile than that with water molecules for reduction and oxidation, respectively [26, 100]. In neutral conditions, however, a different reaction mechanism has been observed [26, 101]. Insufficient hydronium/hydroxyl ion activities at near-neutral pH induced the limiting diffusion currents of reactions with these ions. In this condition, buffering actions are effective based on the reactant switching over varied pH [101]. In addition, for electrochemical measurements, the supporting electrolyte is an essential component for avoiding solution resistance (iR drop). We recently reported a rigorous study on the effect of a supporting electrolyte for electrochemical hydrogen

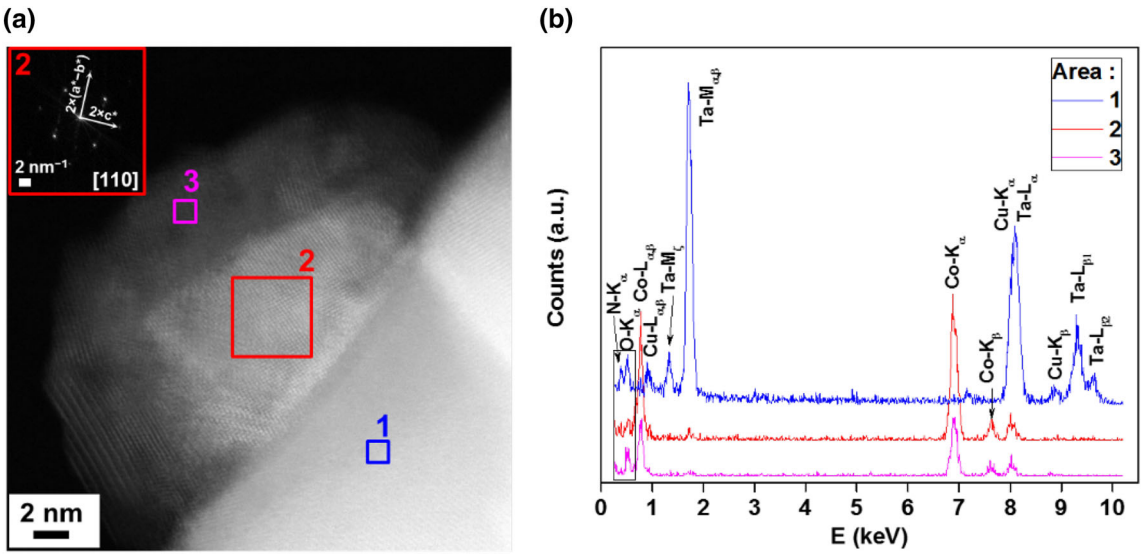

Fig. 7 **a** Dark field HR-STEM for core–shell agglomerated cobalt nanoparticles. The inset shows the FFT results of the core region and depicts a characteristic fcc pattern viewed along the [110] zone axis, **b** X-ray fluorescence spectra of Ta_3N_5 (*1*), the core (*2*) and the shell (*3*) of an agglomerate as depicted on (**a**). *Figures* adapted with permission from [99] Copyright (2015) American Chemical Society

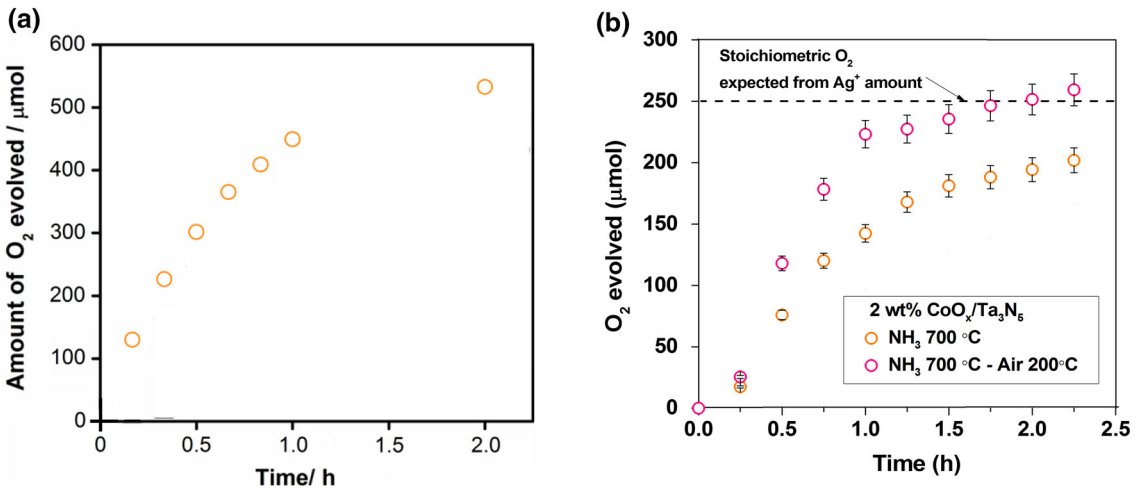

Fig. 8 Time course of photocatalytic OER on **a** 2 wt % CoO_x/Na_2CO_3-Ta_3N_5 nitrided at 500 °C for 1 h, adapted with permission from [42] Copyright (2012) American Chemical Society, and **b** on nitrided 2 wt % CoO_x/Ta_3N_5 with and without oxidation at 200 °C for 1 h, adapted with permission from [99] Copyright (2015) American Chemical Society (**a** 50 and **b** 10 mM $AgNO_3$, at pH 8.5 (La_2O_3 buffer) under visible light irradiation ($420 < \lambda < 800$ nm))

evolution under neutral conditions in a buffered system [102]. However, there is a lack of information available regarding this pH and the electrolyte effect in photocatalytic water splitting.

We attempted to study the photocatalytic OER using CoO_x/Ta_3N_5 at different pH (alkaline conditions) in the presence of 0.1 M $Na_2S_2O_8$ as a sacrificial electron acceptor. Alkaline conditions were selected due to the stability of CoO_x species, which is not stable under neutral or acidic conditions. Hence, selecting a cocatalyst that is stable under a wide range of pH is essential. As shown in Fig. 10, the photocatalytic OER rate increases with increasing pH. The OER rate increases from 40 to 60 µmol h^{-1} for pH 10.5 to pH 12, respectively, and reaches optimum conditions for pH 14 with an OER rate of 100 µmol h^{-1}. This positive trend is associated with improved OER kinetics and a reduced iR drop (solution resistance) for higher pH. A complete study from electrocatalysis and photocatalysis perspectives for different conditions using different catalysts is under development.

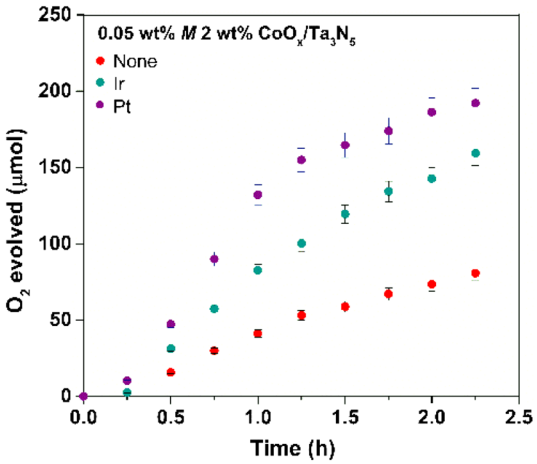

Fig. 9 Time course of photocatalytic OER on CoO_x/Ta_3N_5 (0.1 M $Na_2S_2O_8$, pH 10.5 adjusted with NaOH under visible light irradiation ($420 < \lambda < 800$ nm))

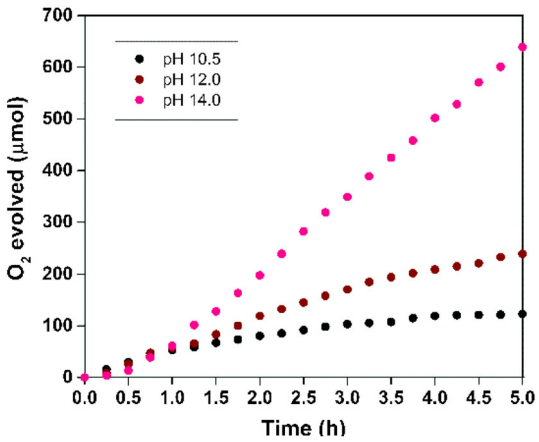

Fig. 10 Time course of photocatalytic OER on CoO_x/Ta_3N_5. (0.1 M $Na_2S_2O_8$, at pH 10.5, 12.0 or 14.0 adjusted with NaOH, under visible light irradiation ($420 < \lambda < 800$ nm))

Kinetics and activation energy measurement for photocatalytic OER using $NiFeO_x$ catalyst

Photocatalytic reaction is essentially electrochemical redox reactions driven by photogenerated electrons and holes in the semiconductor. Our attempt is to study electrochemical reaction apart from semiconductor, and then connect to photophysical process using the semiconductor. For this, we used the $NiFeO_x$ electrocatalyst in alkaline solution as highly active, industrially-vial catalyst [106]. As expected, the catalyst achieved 10 mA cm^{-2} at an overpotential of 260 mV in 1 M of KOH solution and the different temperature measurement resulted in an apparent activation energy of 25 kJ mol^{-1}. The same catalyst was used to decorate Ta_3N_5 powder photocatalyst by applying identical hydrothermal treatment in the presence of Ta_3N_5 powder. The $NiFeO_x/Ta_3N_5$ was used for photocatalytic OER reaction in the presence of 0.1 M $Na_2S_2O_8$ as a strong electron scavenger, thus likely leading to the OER being kinetically relevant. The incorporation of $NiFeO_x$ catalyst leads to fivefold improvement of Ta_3N_5 photocatalytic OER in the visible range with quantum efficiency up to 24 % at 480 nm. The apparent activation energy for photocatalytic OER was found to be 16 kJ mol^{-1}.

The comparison between electrocatalytic and photocatalytic studies [106] shows very strong correlation that the improvement in electrocatalysis leads to similar improvement in photocatalysis. Both electrocatalytic and photocatalytic systems have similar dependence on pH change, where high rates were observed for higher pH. The pH dependence is associated with electrocatalytic kinetics that accordingly influenced the photocatalytic rates. Furthermore, the difference in apparent activation energies for both systems is associated with the possible effects of temperature on the individual thermodynamic and kinetic parameters of the reaction process.

Future directions

Developing efficient visible-light-responsive photocatalysts is essential for making the photocatalytic overall water splitting reaction economically competitive for hydrogen production. To achieve this goal, all the parameters involved in photocatalytic water splitting should be optimized. A collection of theoretical and experimental studies of properties associated with Ta_3N_5 have been utilized to obtain a comprehensive understanding of this material. The fundamental structural and optoelectronic properties of Ta_3N_5 have been addressed. The nitridation is confirmed to proceed via the successive transformation of Ta_2O_5 TaON Ta_3N_5 on the basis of XRD patterns and Rietveld analysis. From the electronic properties, the dielectric constant and effective masses have been calculated. Because of its high dielectric constant and relatively low effective masses, Ta_3N_5 is promising for photocatalytic reaction applications. Studies of lattice dynamics, optical properties, and band positions have been able to clearly show that the synthesized Ta_3N_5 is essentially defective and non-stoichiometric and that a truly pure phase of Ta_3N_5 has never been achieved, even though XRD has shown a pure phase sample. The photophysical properties of Ta_3N_5, such as the absorption coefficient, carrier mobility, and carrier lifetime, have been experimentally measured by synthesizing Ta_3N_5 thin films. Very low kinetic properties with very low transport properties and fast carrier recombination explained why overall water splitting has never been achieved with Ta_3N_5 as a

photocatalyst to date. A surface modification with a cocatalyst and new interface construction are thus suggested to improve the photocatalytic activity. The extent to which the surface states of Ta_3N_5 photocatalysts affect photocatalytic performance has been investigated. The surface topmost layer is demonstrated to play a critical role in the photocatalytic activity of Ta_3N_5; further research on the surface properties of Ta_3N_5 should be conducted to understand and improve charge separation and the resulting photocatalytic activity. Finally, a remarkable improvement in the photocatalytic OER has been achieved with the addition of cobalt as a cocatalyst. There is a trade-off between the optimum contact of hole transfer from bulk Ta_3N_5 to the surface of the cobalt cocatalyst and providing active sites for the electrochemical reaction. Knowing the characteristics of cobalt on the Ta_3N_5 surface, further improvement was attempted by adding a noble metal to the CoO_x/Ta_3N_5 photocatalyst system, where a synergetic effect of CoO_x and noble metals was observed. Although a solar energy to hydrogen conversion efficiency of greater than 1 % using Ta_3N_5 has been achieved, substantial bias in the PEC configuration or the use of a sacrificial reagent is still mandatory. As mentioned in the beginning of this part, the main limitation for Ta_3N_5 is that we cannot make it until now chemically stoichiometric and without crystalline defects. The ammonia treatment necessary for the production of Ta_3N_5 is an aggressive treatment and induces many defects in the crystalline structure that act as sites of charge carrier recombination in the material. Developing new synthesis techniques or new in situ methods of the growth control for Ta_3N_5 is predicted to be able to produce better chemical stoichiometry and improve the crystalline structuration of the material (like epitaxial growth). It can be a key to overcome the Ta_3N_5 limitations and make it efficient for overall water splitting. On the other hand, developing efficient cocatalysts with new deposition techniques for surface functionalization can help to improve the photocatalytic efficiency of Ta_3N_5. Research should continue as the efficiency has not yet reached the desired level. However, a thorough understanding of all the processes involved in the photocatalytic process would pin down the crucial parameters, which will lead to the design of photocatalysts for solving targeted problems.

References

1. Bard, A., Fox, M.A.: Artificial photosynthesis: solar splitting of water to hydrogen and oxygen. Acc. Chem. Res. **28**, 141–145 (1995). doi:10.1021/ar00051a007
2. Khaselev, O., Turner, J.A.: Monolithic photovoltaic-photoelectrochemical device for hydrogen production via water splitting. Science. **280**, 425–427 (1998). doi:10.1126/science.280.5362.425
3. Grätzel, M.: Photoelectrochemical cells. Nature **414**, 338–344 (2001). doi:10.1038/35104607
4. Walter, M.G., Warren, E., McKone, J., Boettcher, S., Mi, Q., Santori, E., Lewis, N.: Solar water splitting cells. Chem. Rev. **110**, 6446–6473 (2010). doi:10.1021/cr1002326
5. Nocera, D.: The artificial leaf. Acc. Chem. Res. **45**, 767–776 (2012). doi:10.1021/ar2003013
6. Ismail, A.A., Bahnemann, D.W.: Photochemical splitting of water for hydrogen production by photocatalysis. Solar Energy Mater. Solar Cells. **128**, 85–101 (2014). doi: 10.1016/j.solmat.2014.04.037
7. Takanabe, K., Domen, K.: Toward visible light response: overall water splitting using heterogeneous photocatalysts. Green **1**, 313–322 (2011). doi:10.1515/GREEN.2011.030
8. Takanabe, K., Domen, K.: Preparation of inorganic photocatalytic materials for overall water splitting. Chemcatchem. **4**, 1485–1497 (2012). doi:10.1002/cctc.201200324
9. Fujishima, A., Honda, K.: Electrochemical photolysis of water at a semiconductor electrode. Nature **238**, 37–38 (1972). doi:10.1038/238037a0
10. Sivula, K., Le Formal, F., Gratzel, M.: Solar water splitting: progress using hematite (α-Fe_2O_3) photoelectrodes. Chemsuschem **4**, 432 (2011). doi:10.1002/cssc.201000416
11. Barroso, M., Mesa, C.A., Pendlebury, S.R., CowanAJ, Hisatomi T., Sivula, K., Grätzel, M., Klug, D.R., Durrant, J.R.: Dynamics of photogenerated holes in surface modified α-Fe_2O_3 photoanodes for solar water splitting. PNAS **109**, 5640 (2012). doi:10.1073/pnas.1118326109
12. Abdi, F.F., Han, L., Smets, A., Zeman, M., Dam, B., van de Krol, R.: Efficient solar water splitting by enhanced charge separation in a bismuth vanadate-silicon tandem photoelectrode. Nat. Commun. **4**, 2195 (2013). doi:10.1038/ncomms3195
13. Kim, T.W., Choi, K.-S.: Nanoporous $BiVO_4$ photoanodes with dual-layer oxygen evolution catalysts for solar water splitting. Science **343**, 990 (2014). doi:10.1126/science.1246913
14. Solarska, R., Jurczakowski, R., Augustynski, J.: A highly stable, efficient visible-light driven water photoelectrolysis system using a nanocrystalline WO_3 photoanode and a methane sulfonic acid electrolyte. Nanoscale **4**, 1553 (2012). doi:10.1039/c2nr11573e
15. Seabold, J.A., Choi, K.S.: Effect of a cobalt-based oxygen evolution catalyst on the stability and the selectivity of photooxidation reactions of a WO_3 photoanode. Chem. Mater. **23**, 1105–1112 (2011). doi:10.1021/cm1019469
16. Higashi, M., Domen, K., Abe, R.: Highly stable water splitting on oxynitride TaON photoanode system under visible light irradiation. J. Am. Chem. Soc. **13**, 46968 (2012). doi:10.1021/ja302059g
17. Kubota, J., Domen, K.: Photocatalytic water splitting using oxynitride and nitride semiconductor powders for production of solar hydrogen. Electrochem. Soc. Interface Summer, **22**(2), 57–62 (2013). doi: 10.1149/2.F07132if
18. Maeda, K., Domen, K.: New non-oxide photocatalysts designed for overall water splitting under visible light. J. Phys. Chem. C **111**, 7851–7861 (2007). doi:10.1021/jp070911w

19. Chun, W.J., Ishikawa, A., Fujisawa, H., Takata, T., Kondo, J.N., Hara, M., Kawai, M., Matsumoto, Y., Domen, K.: Conduction and valence band positions of Ta_2O_5, TaON, and Ta_3N_5 by UPS and electrochemical methods. J. Phys. Chem. B **107**, 1798–1803 (2003). doi:10.1021/jp027593f
20. Li, Y., Takata, T., Cha, D., Takanabe, K., Minegishi, T., Kubota, J., Domen, K.: Vertically aligned Ta_3N_5 nanorod arrays for solar-driven photoelectrochemical water splitting. Adv. Mater. **25**, 125–131 (2013). doi:10.1002/adma.201202582
21. Li, Y., Zhang, L., Torres-Pardo, A., Gonzalez-Calbet, J.M., Ma, Y., Oleynikov, P., Terasaki, O., Asahina, S., Shima, M., Cha, D., Zhao, L., Takanabe, K., Kubota, J., Domen, K.: Cobalt phosphate-modified barium-doped tantalum nitride nanorod photoanode with 1.5% solar energy conversion efficiency. Nat. Commun. (2013). doi:10.1038/ncomms3566
22. Gao, R., Hu, L., Chen, M., Wu, L.: Controllable fabrication and photoelectrochemical property of multilayer tantalum nitride hollow sphere-nanofilms. Small **10**, 3038–3044 (2014). doi:10.1002/smll.201303873
23. Liu, G., Shi, J., Zhang, F., Chen, Z., Han, J., Ding, C., Chen, S., Wang, Z., Han, H., Li, C.A.: Tantalum nitride photoanode modified with a hole-storage layer for highly stable solar water splitting. Angew. Chem. Int. Ed. **53**, 7295 (2014). doi:10.1002/anie.201404697
24. Cong, Y., Park, H.S., Dang, H.X., Fan, F.-R.F., Bard, A.J., Mullins, C.B.: Tantalum cobalt nitride photocatalysts for water oxidation under visible light. Chem. Mater. **24**, 579–586 (2012). doi:10.1021/cm203269n
25. Tong, H., Ouyang, S., Bi, Y., Umezawa, N., Oshikiri, M., Ye, J.: Nano-photocatalytic materials: possibilities and challenges. J. Adv. Mater. **24**, 229–251 (2012). doi:10.1002/adma.201102752
26. Takanabe, K.: Solar water splitting using semiconductor photocatalyst powders. Top Curr. Chem. (2015). doi:10.1007/128_2015_646. **(In press)**
27. Maeda, K., Domen, K.: Photocatalytic water splitting: recent progress and future challenges. J. Phys. Chem. Lett. **1**, 2655–2661 (2010). doi:10.1021/jz1007966
28. Kudo, A., Miseki, Y.: Heterogeneous photocatalyst materials for water splitting. Chem. Soc. Rev. **38**, 253–278 (2009). doi:10.1039/B800489G
29. Abe, R.: Recent progress on photocatalytic and photoelectrochemical water splitting under visible light irradiation. J. Photochem. Photobiol. C **11**, 179–209 (2010). doi:10.1016/j.jphotochemrev.2011.02.003
30. Osterloh, F.E.: Inorganic materials as catalysts for photochemical splitting of water. Chem. Mater. **20**, 35 (2008). doi:10.1021/cm7024203
31. Osterloh, F.E.: Inorganic nanostructures for photoelectrochemical and photocatalytic water splitting. Chem. Soc. Rev. **42**, 2294–2320 (2013). doi:10.1039/c2cs35266d
32. Kakuta, N., Park, K.H., Finlayson, M.F., Ueno, A., Bard, A.J., Campion, A., Fox, M.A., Webber, S.E., White, J.M.: Photoassisted hydrogen production using visible light and coprecipitated ZnS·CdS without a noble metal. J. Phys. Chem. **89**, 732–734 (1985). doi:10.1016/j.solmat.2014.04.037
33. Reber, J.F., Rusek, M.: Photochemical hydrogen production with platinized suspensions of cadmium sulfide and cadmium zinc sulfide modified by silver sulfide. J. Phys. Chem. **90**, 824 (1985). doi:10.1021/j100251a002
34. Xing, C., Zhang, V., Yan, W., Guo, L.: Band structure-controlled solid solution of Cd_{1-x} Zn_xS photocatalyst for hydrogen production by water splitting. Int. J. Hydrog. Energy **31**, 2018 (2006). doi:10.1016/j.ijhydene.2006.02.003
35. Bao, N., Shen, L., Takata, T., Domen, K.: Self-templated synthesis of nanoporous CdS nanostructures for highly efficient photocatalytic hydrogen production under visible light. Chem. Mater. **20**, 110 (2008). doi:10.1021/cm7029344
36. Matsumura, M., Saho, Y., Tsubomura, H.: Photocatalytic hydrogen production from solutions of sulfite using platinized cadmium sulfide powder. J. Phys. Chem. **87**(20), 3807–3808 (1983). doi:10.1021/j100243a005
37. Darwent, J.R., Mills, A.: Photo-oxidation of water sensitized by WO_3 powder. J. Chem. Soc. Faraday Trans. **78**(2), 359–367 (1982). doi:10.1039/F29827800359
38. Erbs, W., Desilvestro, J., Borgarello, E., Gratzel, M.: Visible-light-induced oxygen generation from aqueous dispersions of tungsten(VI) oxide. J. Phys. Chem. **88**, 4001–4006 (1984). doi:10.1021/j150662a028
39. Hara, M., Hitoki, G., Takata, T., Kondo, J.N., Kobayashi, H., Domen, K.: TaON and Ta_3N_5 as new visible light driven photocatalysts. Catal. Today **78**, 555–560 (2003). doi:10.1016/S0920-5861(02)00354-1
40. Hitoki, G., Ishikawa, A., Takata, T., Kondo, J.N., Hara, M., Domen, K.: Ta_3N_5 as a novel visible light-driven photocatalyst ($\lambda < 600$ nm). Chem. Lett. **7**, 736–737 (2002). doi:10.1246/cl.2002.736
41. Ziani, A., Nurlaela, E., Dhawale, D.S., Silva, D.A., Alarousu, E., Mohammed, O.F., Takanabe, K.: Carrier dynamics of a visible-light responsive Ta_3N_5 photoanode for water oxidation. Phys. Chem. Chem. Phys. **17**, 2670–2677 (2015). doi:10.1039/c4cp05616g
42. Ma, S.S.K., Hisatomi, T., Maeda, K., Moriya, Y., Domen, K.: Enhanced water oxidation on Ta_3N_5 photocatalysts by modification with alkaline metal salts. J. Am. Chem. Soc. **134**, 19993–19996 (2012). doi:10.1021/ja3095747
43. Nurlaela, E., Ould-Chikh, S., Harb, M., del Gobbo, S., Aouine, M., Puzenat, E., Sautet, P., Domen, K., Basset, J.-M., Takanabe, K.: Critical role of the semiconductor—electrolyte interface in photocatalytic performance for water-splitting reactions using Ta_3N_5 particles. Chem. Mater. **26**, 4812–4825 (2014). doi:10.1021/cm502015q
44. Harb, M., Sautet, P., Nurlaela, E., Raybaud, P., Cavallo, L., Domen, K., Basset, J.-M., Takanabe, K.: Tuning the properties of visible-light-responsive tantalum (oxy)nitride photocatalysts by non-stoichiometric compositions: a first-principle viewpoint. Phys. Chem. Chem. Phy. **16**, 20548–20560 (2014). doi:10.1039/c4cp03594a
45. Yuliati, L., Yang, J.H., Wang, X., Maeda, K., Takata, T., Antonietti, M., Domen, K.: Highly active tantalum(V) nitride nanoparticles prepared from a mesoporous carbon nitride template for photocatalytic hydrogen evolution under visible lght irradiation. J. Mater. Chem. **20**, 4295–4298 (2010). doi:10.1039/C0JM00341G
46. Fukasawa, Y., Takanabe, K., Shimojima, A., Antonietti, M., Domen, K., Okubo, T.: Synthesis of ordered porous graphitic-C_3N_4 and regularly arranged Ta_3N_5 nanoparticles by using self-assembled silica nanospheres as a primary template. Chem. Asian J. **6**, 103–109 (2011). doi:10.1002/asia.201000523
47. Liu, X., Zhao, L., Domen, K., Takanabe, K.: Photocatalytic hydrogen production using visible-light-responsive Ta_3N_5 photocatalyst supported on monodisperse spherical SiO_2 particulates. Mater. Res. Bull. **49**, 58–65 (2014). doi:10.1016/j.materresbull.2013.08.069
48. Hara, M., Chiba, E., Ishikawa, A., Takata, T., Kondo, J.N., Domen, K.: Ta_3N_5 and TaON thin films on Ta foil: surface composition and stability. J. Phys. Chem. B **107**, 13441–13445 (2003). doi:10.1021/jp036189t
49. Ishikawa, A., Takata, T., Kondo, J.N., Hara, M., Domen, K.: Electrochemical behavior of thin Ta_3N_5 semiconductor film. J. Phys. Chem. B **108**, 11049–11053 (2004). doi:10.1021/jp048802u

50. Li, M., Luo, W., Cao, D., Zhao, X., Li, Z., Yu, T., Zou, Z.: A Co-catalyst-loaded Ta_3N_5 photoanode with a high solar photocurrent for water splitting upon facile removal of the surface layer. Angew. Chem. Int. Ed. **52**, 11016–11020 (2013). doi:10.1002/anie.201305350
51. Armytage, D., Fender, B.E.F.: Anion ordering in TaON: a powder neutron-diffraction investigation. Acta Cryst. Sect. B **30**(3), 809–812 (1974). doi:10.1107/S0567740874003761
52. Dabirian, A., van de Krol, R.: High-temperature ammonolysis of thin film Ta_2O_5 photoanodes evolution of structural, optical, and photoelectrochemical properties. Chem. Mater. **27**, 708–715 (2015). doi:10.1021/cm503215p
53. Reuter, K., Scheffler, M.: Composition, structure, and stability of RuO_2 (110) as a function of oxygen pressure. Phys. Rev. B **65**, 035406 (2001). doi:10.1103/PhysRevB.65.035406
54. Reuter, K., Scheffler, M.: Composition and structure of the RuO_2 (110) surface in an O_2 and CO environment: implications for the catalytic formation of CO_2. Phys. Rev. B **68**, 045407 (2003). doi:10.1103/PhysRevB.68.045407
55. Henderson, S.J., Hector, A.L.: Structural and compositional variations in Ta_3N_5 produced by high temperature ammonolysis of tantalum oxide. J. Solid State Chem. **179**, 3518–3524 (2006). doi:10.1016/j.jssc.2006.07.021
56. Brus, L.E.J.: A simple model for the ionization potential, electron affinity, and aqueous redox potentials of small semiconductor crystallites. J. Chem. Phys. **79**, 5566–5571 (1983). doi:10.1063/1.445676
57. Ekimov, A.I., Onushchenko, A.A.: Size quantization of the electron energy spectrum in a microscopic semiconductor crystal. JETP Lett. **40**, 1136–1139 (1984)
58. Ho, C.-H., Ke-B, Low, Klie, R.F., Maeda, K., Domen, K., Meyer, R.J., Snee, P.T.: Synthesis and characterization of semiconductor tantalum nitride nanoparticles. J. Phys. Chem. C **115**, 647–652 (2011). doi:10.1021/jp110105u
59. Gao, Q., Wang, S., Ma, Y., Tang, Y., Giordano, C., Antonietti, M.: SiO_2-surface-assisted controllable synthesis of TaON and Ta_3N_5 nanoparticles for alkene epoxidation. Angew. Chem. Int. Ed. **51**, 961–965 (2012). doi:10.1002/anie.201107216
60. Pinaud, B.A., Vesborg, P.C.K., Jaramillo, T.F.: Effect of film morphology and thickness on charge transport in Ta_3N_5/Ta photoanodes for solar water splitting. J. Phys. Chem. C **116**, 15918–15924 (2012). doi:10.1021/jp3041742
61. Feng, X., La Tempa, T., Basham, J., Mor, G., Varghese, O., Grimes, C.: Ta_3N_5 nanotube arrays for visible light water photoelectrolysis. Nano Lett. **10**, 948–952 (2010). doi:10.1021/nl903886e
62. Yokoyama, D., Hashiguchi, H., Maeda, K., Minegishi, T., Takata, T., Abe, R., Kubota, J., Domen, K.: Ta_3N_5 photoanodes for water splitting prepared by sputtering. Thin Solid Films **519**, 2087–2092 (2011). doi:10.1016/j.tsf.2010.10.055
63. Brese, N., O'Keeffe, M.: The structure of Ta_3N_5 at 16 K by time-of-flight neutron diffraction. Acta Cryst. C **47**, 2291–2294 (1991)
64. Nurlaela, E., Harb, M., del Gobbo, S., Vashishta, M., Takanabe, K.: Combined experimental and theoretical assessments of the lattice dynamics and optoelectronics of TaON and Ta_3N_5. J. Solid State Chem. **229**, 219–227 (2015). doi:10.1016/j.jssc.2015.06.029
65. Gajdoš, M., Hummer, K., Kresse, G., Furthmüller, J., Bechstedt, F.: Linear optical properties in the projector-augmented wave methodology. Rev. B, Phys (2006). doi:10.1103/PhysRevB.73.045112
66. Le Bahers, T., Rérat, M., Sautet, P.: Semiconductors used in photovoltaic and photocatalytic devices: assessing fundamental properties from DFT. J. Phys. Chem. C **118**, 5997–6008 (2014)
67. Morbec, J.M., Narkeviciute, I., Jaramillo, T.F., Galli, G.: Optoelectronic properties of Ta_3N_5: a joint theoretical and experimental study. Phys. Rev. B **90**, 155204 (2014). doi:10.1103/PhysRevB.90.155204
68. Watanabe, E., Ushiyama, H., Yamashita, K.: Theoretical studies on the stabilities and reactivities of Ta_3N_5 (1 0 0) surfaces. Chem. Phys. Lett. **561–562**, 57–62 (2013). doi:10.1016/j.cplett.2012.12.068
69. Wang, J., Feng, J., Zhang, L., Li, Z., Zou, Z.: Role of oxygen impurity on the mechanical stability and atomic cohesion of Ta_3N_5 semiconductor photocatalyst. Phys. Chem. Chem. Phys. **16**, 15375 (2014). doi:10.1039/C4CP00120F
70. Wang, J., Fang, T., Zhang, L., Feng, J., Li, Z., Zou, Z.: Effects of oxygen doping on optical band gap and band edge positions of Ta_3N_5 photocatalyst: A GGA + U calculation. J. Catal. **309**, 291–299 (2014). doi:10.1016/j.jcat.2013.10.014
71. Lacomba-Perales, R., Martinez-García, D., Errandonea, D., Le Godec, Y., Philippe, J., Le Marchand, G., Chervin, J.C., Polian, A., Múñoz, A., López-Solano, : Experimental and theoretical investigation of the stability of the monoclinic BaWO4-II phase at high pressure and high temperature. J. Phys. Rev. B **8**, 144117 (2010)
72. Quarti, C., Grancini, G., Mosconi, E., Bruno, P., Ball, J.M., Lee, M.M., Snaith, H.J., Petrozza, A.M., Angelis, F.D.: The Raman spectrum of the $CH_3NH_3PbI_3$ hybrid perovskite: interplay of theory and experiment. J. Phys. Chem. Lett. **5**, 279–284 (2014)
73. Dabirian, A., Van de Krol, R.: Resonant optical absorption and defect control in Ta_3N_5 photoanodes. Appl. Phys. Lett. **102**, 033905 (2013). doi:10.1063/1.4788930
74. Harb, M., Cavallo, L., Basset, J.-M.: Major difference in visible-light photocatalytic features between perfect and self-defective Ta_3N_5 materials a screened coulomb hybrid DFT investigation. J. Phys. Chem. C **118**, 20784–20790 (2014). doi:10.1021/jp506066p
75. Khan, S., Zapata, M.J.M., Preira, M.B., Gonçalves, R.V., Strizik, L., Dupont, J., Santos, M.J.L., Teixeira, S.R.: Structural, optical and photoelectrochemical characterizations of monoclinic Ta_3N_5 thin films. Phys. Chem. Chem. Phys. Accept. (2015). doi:10.1039/x0xx00000x
76. Inoue, Y.: Photocatalytic water splitting by RuO_2-loaded metal oxides and nitrides with d^0- and d^{10}-related electronic configurations. Energy Environ. Sci. **2**, 364 (2009). doi:10.1039/B816677N
77. Reshak, A.H.: Electronic structure and dispersion of optical function of tantalum nitride as a visible light photo-catalyst. Comp. Mater. Sci. **89**, 45 (2014). doi:10.1016/j.commatsci.2014.03.035
78. El-Nahass, M.M., Youssef, T.E.: Influence of X-ray irradiation on the optical properties of ruthenium(II)octa-(n-hexyl)-phthalocyanine thin film. J. Alloys Compd **503**, 86–91 (2010). doi:10.1016/j.jallcom.2010.04.029
79. Vurgaftman, I., Meyer, J.R., Ram-Mohan, L.R.: Band parameters for III–V compounds semiconductors and their alloys. J. Appl. Phys. **89**, 5815–5875 (2001). doi:10.1063/1.1368156
80. Taguchi, T., Shirafuji, J., Inuishi, Y.: Excitonic emission in cadmium telluride. Phys. Status Solidi B **68**, 727–738 (1975). doi:10.1002/pssb.2220680234
81. Young, K.F., Frederikse, H.P.R.: Compilation of static dielectric constant of inorganics solids. J. Phys. Chem. Ref. Data **409**, 2313 (1973)
82. Gilleo, M.A., Bailey, P.T., Hill, D.E.: Free-carrier and exciton recombination radiation in GaAs. Phys. Rev. **174**, 898–905 (1968). doi:10.1103/PhysRev.174.898
83. Madelung, O.: Semiconductors: data handbook, 3rd edn. Springer, New York (2004)

84. Adashi, S.: GaAs and related materials. World Scientific Publishing Co. Pte. Ltd, Singapore (1994)
85. Zeiri, L., Patla, I., Acharya, S., Golan, Y., Efrima, S.: Raman spectroscopy of ultranarrow CdS nanostructures. J. Phys. Chem. C **111**, 11843–11848 (2007). doi:10.1021/jp072015q
86. Furube A, Maeda K, Domen K Transient absorption study on photogenerated carrier dynamics invisible light responsive photocatalysts GaN:ZnO. Proc of SPIE 2011 8109 810904
87. Chen, Z., Jaramillo, T.F., Deutsch, T.G., Kleiman-Shwarsctein, A., Forman, A.J., Gaillard, N., Garland, R., Takanabe, K., Heske, C., Sunkara, M., McFarland, E.W., Domen, K., Miller, E.L., Turner, J.A., Dinh, H.N.: Accelerating materials development for photoelectrochemical hydrogen production: standards for methods, definitions, and reporting protocols. J. Mater. Res. **25**, 3–16 (2010). doi:10.1557/JMR.2010.0020
88. Esswein, A.J., McMurdo, M.J., Ross, P.N., Bell, A.T., Tilley, T.D.: Size-dependent activity of Co_3O_4 nanoparticle anodes for alkaline water electrolysis. J. Phys. Chem. C **113**, 15068–15072 (2009). doi:10.1021/jp904022e
89. Gorlin, Y., Chung, C.-J., Nordlund, D., Clemens, B.M.: Electrocatalytic oxygen evolution reaction (OER) on Ru, Ir, and Pt catalysts: a comparative study of nanoparticles and bulk materials. ACS Catal. **2**, 1765–1772 (2012). doi:10.1021/cs3003098
90. Deng, X., Tüysüz, H.: Cobalt-oxide-based materials as water oxidation catalyst: recent progress and challenges. ACS Catal. **4**, 3701–3714 (2014). doi:10.1021/cs500713d
91. Yeo, B.S., Bell, A.T.: Enhanced activity of gold-supported cobalt oxide for the electrochemical evolution of oxygen. J. Am. Chem. Soc. **133**, 5587–5593 (2011). doi:10.1021/ja200559j
92. Liao, M., Feng, J., Luo, W., Wang, Z., Zhang, J., Li, Z., Yu, T., Zou, Z.: Co_3O_4 nanoparticles as robust water oxidation catalysts towards remarkably enhanced photostability of a Ta_3N_5 photoanode. Adv. Funct. Mater. **22**, 3066–3074 (2012). doi:10.1002/adfm.201102966
93. Kasahara, A., Nukumizu, K., Hitoki, G., Takata, T., Kondo, J.N., Hara, M., Kobayashi, H., Domen, K.: Photoreactions on $LaTiO_2N$ under visible light irradiation. J. Phys. Chem. A **106**, 6750–6753 (2002). doi:10.1021/jp025961
94. Higashi, M., Domen, K., Abe, R.: Fabrication of an efficient $BaTaO_2N$ photoanode harvesting a wide range of visible light for water splitting. J. Am. Chem. Soc. **135**, 10238–10241 (2013). doi:10.1021/ja404030x
95. Ran, J., Zhang, J., Yu, J., Jaroniecc, M., Qiao, S.Z.: Earth-abundant cocatalysts for semiconductor based photocatalytic water splitting. Chem. Soc. Rev. **43**, 7787–7812 (2014). doi:10.1039/c3cs60425j
96. Zhong, D.K., Choi, S., Gamelin, D.R.: Near-complete suppression of surface recombination in solar photoelectrolysis by "Co-Pi" catalyst-modified W:biVO$_4$. J. Am. Chem. Soc. **133**, 18370–18377 (2011). doi:10.1021/ja207348x
97. Barroso, M., Cowan, A.J., Pendlebury, S.R., Gratzel, M., Klug, D.R., Durrant, J.R.: The role of cobalt phosphate in enhancing the photocatalytic activity of α-Fe_2O_3 toward water oxidation. J. Am. Chem. Soc. **1331**, 4868–14871 (2011). doi:10.1021/ja205325v
98. Long, M., Cai, W., Kisch, H.: Visible light induced photoelectrochemical properties of n-BiVO$_4$ and n-BiVO$_4$/p-Co_3O_4. J. Phys. Chem. C **112**, 548–554 (2008). doi:10.1021/jp075605x
99. Nurlaela, E., Ould-Chikh, S., Llorens, I., Hazemann, JL., Takanabe, K.: Establishing efficient cobalt based catalytic sites for oxygen evolution on Ta_3N_5 photocatalyst. Chem. Mater. **27**, 5685–5694 (2015). doi:10.1021/acs.chemmater.5b02139
100. Shinagawa, T., Takanabe, K.: Identification of intrinsic catalytic activity for electrochemical reduction of water molecules to generate hydrogen. Phys. Chem. Chem. Phys. **17**, 15111–15114 (2015). doi:10.1039/c5cp02330k
101. Shinagawa, T., Takanabe, K.: Electrocatalytic hydrogen evolution under densely buffered neutral pH conditions. J. Phys. Chem. C **119**, 20453–20458 (2015). doi:10.1021/acs.jpcc.5b05295
102. Shinagawa, T., Takanabe, K.: Impact of solute concentration on the electrocatalytic conversion of dissolved gases in buffered solutions. J. Power Sources **287**, 465–471 (2015). doi:10.1016/j.jpowsour.2015.04.091
103. Abdi, F., Savenije, T., May, M., Dam, B., van de Krol, R.: The origin of slow carrier transport in BiVO$_4$ thin film photoanodes: a time-resolved microwave conductivity study. J. Phys. Chem. Lett. **4**, 2752 (2013). doi:10.1021/jz4013257
104. Joly, A.G., Williams, J.R., Chambers, S.A., Xiong, G., Hess, W.P., Laman, D.M.: Carrier dynamics in α-Fe2O3 (0001) thin films and single crystals probed by femtosecond transient absorption and reflectivity. J. Appl. Phys. **99**, 053521 (2006). doi:10.1063/1.2177426
105. Shinde, S.S., Bansode, R.A., Bhosale, C.H., Rajpure, K.Y.: Physical properties of hematite α-Fe_2O_3 thin films: application to photoelectrochemical solar cells. J. Semicond. **32**, 013001 (2011). doi:10.1088/1674-4926/32/1/013001
106. Nurlaela, E., Shinagawa, T., Qureshi, M., Dhawale, D.S., Takanabe, K.: Temperature dependence of electrocatalytic and photocatalytic oxygen evolution reaction rates using NiFe oxide. ACS Catal. **6**, 1713 (2016). doi:10.1021/acscatal.5b02804